Gulf Stream Simulations and the Dynamics of Ring and Meander Processes

ALLAN R. ROBINSON, MICHAEL A. SPALL AND NADIA PINARDI

Center for Earth and Planetary Physics, Harvard University, Cambridge, Massachusetts

(Manuscript received 2 July 1987, in final form 25 April 1988)

ABSTRACT

We present here a regional, eddy resolving, numerical study of the dynamics of Gulf Stream Meander and Ring (GSMR) interaction processes. We initialize the Harvard quasi-geostrophic open-boundary model with realistic meander and ring locations as indicated by remotely sensed sea surface temperature (SST) data and predict the flow evolution for the period 23 November to 19 December 1984. The methodology of Feature–Model initialization is introduced to extend the surface information to the thermocline and deep levels in terms of climatological structures, which are then dynamically adjusted by the model. Six numerical simulations are carried out to explore the influence of initial and boundary conditions on the flow evolution. All of the major events observed in the SST data are simulated, including the birth of new warm and cold core rings. The results show the relevance of quasi-geostrophic dynamics for the GSMR region on these time scales in the thermocline. A set of parameter and sensitivity experiments then elucidate the dependence on physical parameters; ring births are nonlinear baroclinic processes. The dynamics of these realistic cold and warm core formation events are quantified via local energy and vorticity budget analyses (EVA). The cold core case involves a process of nonlinear baroclinic cascades that convert available gravitational energy to kinetic energy and vice versa. The warm core case involves a differential horizontal advection process.

1. Introduction

The Gulf Stream Meander and Ring (GSMR) region from Cape Hatteras eastward to the Grand Banks represents one of the most interesting areas of the world ocean for dynamical research. Current flow is strong, mesoscale variability is energetic, and major features are coherently structured. Meanders grow, propagate, amplify, distend, and snap off, forming cold and warm ring–current eddies. The rings, free to roam into the Sargasso Sea to the south but trapped to the north between the stream and the continental slope, interact with the stream and its meanders exhibiting coalescence and merger events with transient and permanent characteristics and involving both warm and cold cores. Multiple ring–ring and ring–stream interactions occur. The local vorticity dynamics of GSMR processes, generally not yet known in their own right, can reasonably be expected also to have generalizable aspects relevant to the dynamics of related current regions (e.g., Kuroshio, etc.). Moreover, contributions to the understanding of fundamental vortex processes in fluid dynamics are also possible. A knowledge of the statistics of the dynamics of the GSMR region and of the interaction of this region with the larger flow in which it is embedded is necessary for understanding and modelling the North Atlantic general circulation.

Corresponding author address: Prof. Allan R. Robinson, Center for Earth and Planetary Physics, Pierce Hall, Harvard University, Cambridge, MA 02138.

The accurate and complete field realizations required for local dynamical studies imply a shared methodological basis with optimal field estimation studies for nowcasting and forecasting of ocean currents and related fields. The GSMR region, because of its location and because of the strength of its mesoscale variability, is particularly interesting for practical forecasts related to marine operations, resource management, weather and climate, and large scale environmental management. Such forecasts and predictions useful for efficient mesoscale dynamical experimentation have of course a real time requirement. Data assimilation, the melding of observations with dynamical model predictions, provides hindcasts, nowcasts and forecasts on the one hand and utilizes dynamical interpolation and dynamically filtered fields on the other. The highly structured fields of the GSMR region and the inhomogeneity and nonstationarity of their statistics require special objective analysis, gridding and initialization and updating techniques. Finally, we mention that satellite signals [infrared sensed sea surface temperature (SST) and altimeter sea surface height (SSH)] are strong in the GSMR region so that satellite data assimilation studies there can usefully precede those for weaker signal regions.

The present study uses the Harvard open ocean dynamical model for about a month's simulation during an active period of ring formation and interactions in the GSMR region. The simulation is baroclinic and quasigeostrophic with 15 km resolution horizontally and six levels in the vertical. The simulation and its

verification and assessment are based on sea surface temperature (SST) maps for late November and December 1984 obtained from NOAA analyses primarily derived from satellite borne sensors (McHugh and Clark 1984). Dynamical model initialization based upon real data is involved but not data assimilation via updating. The methodology introduced for initialization involves locating by satellite IR data the position of major features, i.e., the thermal fronts associated with the Gulf Stream axis and with rings, and then fitting "Feature–Models" in place under them. Feature–Models represent the well-known and enduring shapes and structures of the current and rings in terms of analytical formulas involving only a few discrete indices, which can be set by recent historical knowledge or statistical experience. The dynamical model then dynamically adjusts the features, interacts them and dynamically interpolates between them, and finally evolves the fields forward in time physically. An objective is to see how well the model can do running forward for a few weeks; the answer is encouraging. All major events can be reproduced within the constraints of the observations, although the data is somewhat gappy in space and time. The quasi-geostrophic dynamics is shown to be relevant to the major evolution and interaction processes in the thermocline on these time scales. Our attempt to simulate is carried out in conjunction with idealized studies related to ring generation processes, e.g., simplified boundary conditions are invoked with a reduced number (or no) rings present. The sensitivity of tuning the model to the best values of physical nondimensional parameters is studied by numerical experiments involving variation of those parameters away from their central values. The energy and vorticity analysis (EVA) of processes associated with ring formation is investigated by detailed studies of the balances occurring in cold and warm ring production events. The simulation and its context serve also to calibrate the model for application to GSMR nowcasting and forecasting and provide a realistic set of dynamically filtered fields for benchmark experimental and data assimilation system design studies.

The GSMR region is reviewed by Richardson (1983) and Watts (1983). Relevant to our study is recent modeling work carried out by Ikeda (1981), Ikeda and Apel (1981), and Pratt and Stern (1986) for idealized regional Gulf Stream studies. In our Feature–Model initialization procedures we used the thin jet model developed by Niiler and Robinson (1967) and ring models suggested by Olson (1980) and Joyce (1984). The observational structure and variability of the Gulf Stream front, both from SST and subsurface measurements, is analyzed in detail in Robinson et al. (1974), Bower et al. (1985), and Halkin and Rossby (1985).

Section 2 summarizes the dynamical model, the region of the simulation and the computational parameters. The Feature–Models and the implementation of the initialization technique is presented in section 3, followed in section 4 by the SST data and the descriptive–synoptic oceanography of the region (23 November to 19 December 1984). Section 5 describes the set of six numerical forecast experiments. Section 6 describes a set of physical sensitivity experiments and the EVA of ring production events. Section 7 presents the summary and conclusions.

2. Model equations, parameters, and methodology

The Harvard quasi-geostrophic open boundary model (Miller et al. 1983; Robinson and Walstad 1987) uses the following nondimensional form of the potential vorticity conservation equation

$$\frac{\partial}{\partial t}(\nabla^2\psi + \Gamma^2(\sigma\psi_z)_z) + \alpha J(\psi, \nabla^2\psi) + \alpha\Gamma^2 J(\psi, (\sigma\psi_z)_z) + \beta\psi_x = F_{pqr} \quad (1a)$$

where ψ is the geostrophic streamfunction field, J the Jacobian operator, and

$$\alpha = t_0\frac{V_0}{d},\ \beta = t_0\beta_0 d,\ \Gamma^2 = \frac{f_0^2 d^2}{N_0^2 H^2}\ \sigma = \frac{N_0^2}{N^2(z)}.$$

Here F_{prq} is the symbolic representation of a Shapiro filter operation on the vorticity field, a filter of order p is applied q times every r time steps (Shapiro 1970). Use of the Shapiro filter as a parameterization of subgrid scale processes has been documented for open ocean flows (Robinson and Walstad 1987, section 2.3). The f_0 is the Coriolis parameter at the center of the model domain, β_0 is the variation of f_0 with latitude, $N^2(z)$ is the Brunt–Väisälä frequency, and N_0^2 is the Brunt–Väisälä frequency at mid-thermocline. The time (t_0), velocity (V_0), horizontal (d) and vertical (H) length scales are chosen to be 4 days, 40 cm s^{-1}, 40 km and 700 m. The velocity scale is representative of the thermocline speeds in Gulf Stream current and ring cores (Halkin and Rossby 1985). The time scale of 4 days is associated with the temporal growth of perturbations with an approximate wavelength of 200 km, the fastest meander scale directly observed (Robinson et al. 1974; Watts and Johns 1982). The spatial scale of 40 km is of the order of the Rossby radius of deformation for the region. Table 1 lists the standard values of the model parameters along with the symbolic representations of the various terms in Eq. (1a) (see Eq. 1b below). We call the sum of the relative ($R = \nabla^2\psi$) and thermal [$T = \Gamma^2(\sigma\psi_z)_z$] vorticity the dynamical vorticity Q and distinguish between the time rate of change ($\dot{}$) and advection (ΔF) of R, T, and $P = \beta y$, the planetary vorticity. Equation (1a) can then be written symbolically as

$$\dot{Q} = \dot{R} + \dot{T} = \Delta F_R + \Delta F_T + \Delta F_P + F. \quad (1b)$$

The geostrophic kinetic energy [$K = (u^2 + v^2)/2$] and available gravitational energy [$A = \sigma\Gamma^2(\psi_z^2/2)$] equations consistent with Eq. (1a) are written

TABLE 1. List of symbols and standard model parameters.

Symbols	Definitions
U_0	velocity scale = 40 cm s^{-1}
t_0	time scale = 4 days
d	horizontal scale = 40 km
f_0	Coriolis parameter at $\theta_0 = 39°N$ (9.210^{-5} sec^{-1})
β_0	$\partial f/\partial y\|_{\theta=\theta_0} = 1.8 \times 10^{-11}$ (m s)$^{-1}$
N_0^2	mid-thermocline Brunt–Väisälä frequency value
H	vertical scale = 700 m.
$N^2(z)$	climatological Brunt–Väisälä profile
α	$t_0U_0/d = 3.456$
β	$\beta_0 t_0 d = 0.25$
Γ^2	$f_0^2d^2/N_0^2H^2 = 1.4$
σ	$N_0^2/N^2(z)$, stability profile
ψ	geostrophic streamfunction or pressure
q	dynamical vorticity = $R + T$
R	relative vorticity $\nabla^2\psi$
T	thermal vorticity $\Gamma^2(\sigma\psi_z)_z$
$\dot{R}$	$\partial_t\nabla^2\psi$
$\dot{T}$	$\Gamma^2\partial_t(\sigma\psi_z)_z$
ΔF_R	$-\alpha\mathbf{v}\cdot\nabla\nabla^2\psi$
ΔF_T	$-\alpha\Gamma^2\mathbf{v}\cdot\nabla(\sigma\psi_z)_z$
ΔF_P	$-\beta\psi_x$
F_{pqr}	Shapiro filter ($p = 4$, $q = 2$, $r = 1$)
K	kinetic energy = $(u^2 + v^2)/2$
A	available gravitational energy = $\Gamma^2\sigma(\psi_z^2/2)$
$\dot{K}$	$\partial_t K$
$\dot{A}$	$\partial_t A$
ΔF_K	$-\alpha\nabla\cdot(\mathbf{v}K)$
ΔF_π	$-\nabla\cdot(\psi\nabla\psi_{zt} + \alpha\psi\mathbf{v}\cdot\nabla\nabla\psi + \beta\psi yv)$
δf_π	$\sigma\Gamma^2\partial_z(\psi\psi_{zt} + \psi\mathbf{v}\cdot\nabla\psi_z)$
b	$+\psi_z w$
ΔF_A	$-\alpha\nabla\cdot(\mathbf{v}A)$

$$\frac{\partial}{\partial t}K = -\alpha\nabla\cdot(\mathbf{v}K) + \nabla\cdot(\psi\nabla\psi_t + \alpha\psi\mathbf{v}\cdot\nabla\nabla\psi + \beta\psi\mathbf{v}y) + \frac{\partial}{\partial z}(\Gamma^2\sigma\psi\psi_{zt} + \Gamma^2\alpha\sigma\psi\mathbf{v}\cdot\nabla\psi_z) - \psi_z w + D \quad (2a)$$

or

$$\dot{K} = \Delta F_K + \Delta F_\pi{}^t + \Delta F_\pi{}^a + \Delta F_\pi{}^\beta + \delta f_\pi{}^t + \delta f_\pi{}^a - b + D \quad (2b)$$

and

$$\frac{\partial}{\partial t}A = -\alpha\nabla\cdot(\mathbf{v}A) + \psi_z w + D \quad (3a)$$

or

$$\dot{A} = \Delta F_A + b + D \quad (3b)$$

where the (b) equations are the symbolic representation of the terms in (2a) and (3a), (see Table 1). The D is a dissipation-like term in the energy equations arising from the Shapiro filter operation on the vorticity.

The methodology of energy and vorticity analysis (EVA) applied to the predicted fields from the open boundary quasi-geostrophic model is explained in detail in Pinardi and Robinson (1986) and we assume that the reader is familiar with it. Briefly, it is a local balance analysis performed via a time series of maps of the individual terms in Eqs. (1), (2) and (3) in order to display relevant instantaneous contributions in selected subregions of interest.

The horizontal open boundary conditions in the quasi-geostrophic model are the Charney–Fjortof–VonNeumann boundary conditions, vorticity at inflow points and streamfunction all around the domain. These boundary conditions have been shown to be robust in model forecast experiments (Robinson et al. 1986; Robinson and Walstad 1987).

The two physical boundaries at the sea surface and bottom of the ocean are model interfaces at which the geostrophic perturbation density ($\delta = \psi_z$) is calculated (or specified if constant) and the vertical ageostrophic velocity, w, is specified. The prognostic equation for the perturbation density ψ_z is given by the thermodynamic equation evaluated at the mean surface height or bottom depth

$$-\Gamma^2\sigma\frac{\partial}{\partial t}\psi_z - \alpha\sigma\Gamma^2J(\psi, \psi_z) = w + F_{pqr} \quad (4)$$

where F_{pqr} is the representation of a Shapiro filter operation on ψ_z. To solve Eq. (4) we need to know ψ_z at the initial time and at inflow points on every time step. For the surface we have assumed that $w = 0$ and that the advecting horizontal velocity is given by the underlying (level 1) streamfunction field. Consequently the surface boundary condition has no feedback on the vorticity dynamics in the remaining column of water and the surface density is simply a passive tracer advected by the level 1 geostrophic field. Solving the initial-boundary value problem associated with Eq. (4) does allow a realistic surface outcropping of isopycnals. The vertical velocity at the bottom is obtained through a no-normal flow requirement

$$w = -J(\psi, h)$$

where h is the deviation of the topographic relief from the average depth in the region of interest and the advecting velocity field is extrapolated from the lowest layer ψ.

To implement the model in the Gulf Stream meander and ring formation region we need the mean stratification of the region. We used the NODC dataset (Levitus and Oort 1977) which consists of 33 levels from the surface to the bottom of temperature and salinity values on a one degree grid. The temperature and salinity profiles have been horizontally averaged in a region between 25.5° and 50.5°N, 79.5° and 50.5°W in order to obtain the averaged $N^2(z)$ profile. This region was chosen to give a representative value of N^2 for the entire Gulf Stream meander and ring formation region. When our studies became concentrated in the model domain (shown in Fig. 2), a smaller

domain more representative of the modeled region was sampled. This produced variations only of the order of 5% in magnitude of the eigenvalues of the vertical structure equation. The N^2 profile used in these calculations is shown in Fig. 1a and the first three baroclinic eigenmodes of

$$\Gamma^2(\sigma\phi_{nz})_z = -\lambda^2\phi_{nz}$$

with boundary conditions $\phi_{nz} = 0$ at $z = 0$ and $z = 4500$ m (the average depth of the basin) are shown in Fig. 1b. The eigenvalues for $n = 1, 2, 3$ are 33.75, 15.48, and 12.05 km, respectively, in the continuous limit (50 m vertical resolution). The first baroclinic mode has a zero crossing at about 1230 meters and the second baroclinic mode has zero crossings at 350 m and 2650 m with a relative maximum at 900 m.

The quasi-geostrophic streamfunction may be used along with this mean stratification to derive a consistent temperature profile for a fluid in motion. The density anomaly corresponding to quasi-geostrophic motion may be calculated from ψ_z at each level and horizontal position. Given the reference density and the model density anomaly, the vertical distance by which the density field has been perturbed due to the fluid motion can be calculated. For adiabatic motion, the new temperature at that level can also be calculated from the reference temperature.

The model uses finite differences (or levels) in the vertical and finite elements in the horizontal. The vertical resolution of the model has been chosen to be six levels, located at 100, 300, 700, 1100, 2150 and 3800 m, giving sufficient resolution above, through, and below the main thermocline. This choice of levels insures a good estimate of the modal shape and eigenvalues for the first two baroclinic modes with respect to the continuous limit. The model domain consists of a rectangle 87 × 65 grid points in the x and y directions, centered at 39°N, 59.5°W, and rotated 20 degrees counterclockwise from an east by north orientation. The grid resolution is 15 km which gives a total domain size of 1290 km × 960 km. The model runs presented here use a 1-hour time step and a fourth-order Shapiro filter applied twice every time step on the vorticity field and on the perturbation density at the bottom and top interfaces.

The model domain and full topography are shown in Fig. 2. The northern boundary has been aligned with the shelf break, modelled as a vertical wall. Because high, steep mountains could violate the quasigeostrophic approximation, the New England Seamounts, which are located within the domain, have been truncated at 5000 m in the model topography, i.e., they are simply removed and replaced by the mean depth of the surrounding abyssal plain. Removing the seamounts of course removes a possible important topographic interaction in this region. However, our simulations give interestingly realistic results carried out for about a 4 week period. The initial distribution of eddies and the stream (see section 4 below) may of course already reflect seamount effects. Comparison calculations, not reported here, were performed with seamounts truncated at 2000 m or truncated at 5000 m but with a vortex stretching term due to the full slope effect. Little change occurred over two week experiments.

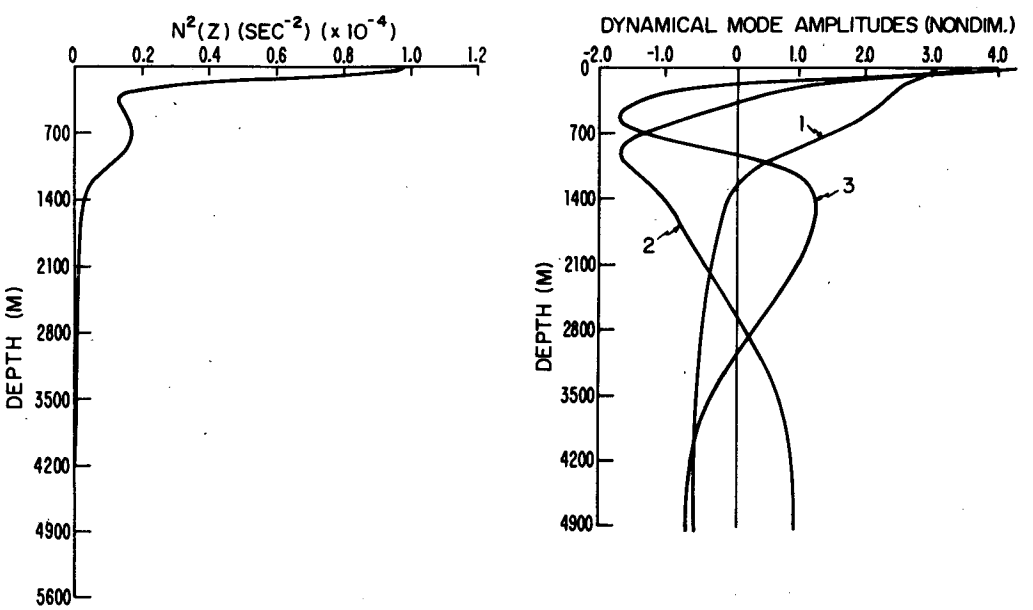

FIG. 1. (a) $N^2(z)$ for the Gulf Stream region. (b) Dynamical modes for the Gulf Stream $N^2(z)$; first, second, and third baroclinic modes are indicated by 1, 2, 3, respectively.

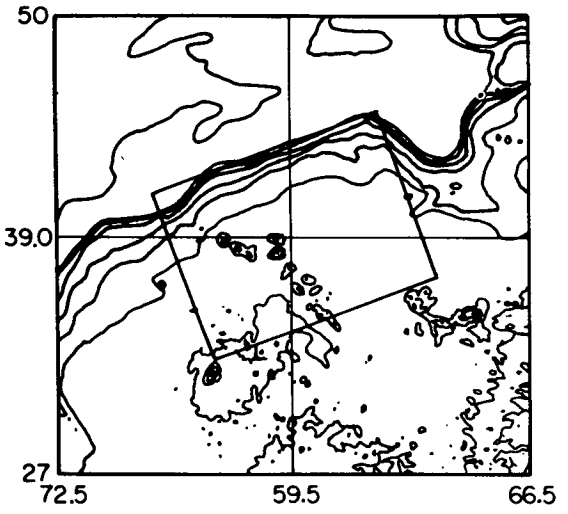

FIG. 2. Model domain (1290 × 960 km) superimposed on the local bottom topography, maximum depth: 6000 m, contour interval: 800 m.

3. Feature model initialization

Here we describe the methodology of using sea surface temperature (SST) data from infrared satellite sensors (AVHRR) to determine initial and boundary conditions for the open boundary model. It is believed that the sharp horizontal gradient in the sea surface temperature (thermal front) delineates the subsurface Gulf Stream front on the spatial scale of a few hundred kilometers or higher. Robinson et al. (1974) showed that there is little relative motion between near surface buoys and the "thermal path" of the Gulf Stream as seen by the satellite SST maps. The Feature-Model initialization methodology utilizes (i) SST to locate the surface fronts associated with the positions of the stream axis and of any rings that may be present, (ii) Feature-Models based on previous subsurface measurements to generate first estimates of subsurface profiles, and (iii) the dynamical model itself to adjust and interact the features and to interpolate between the features. Although the flow in the meander and ring formation region is quite complicated, experience indicates that the Gulf Stream viewed in its own natural coordinate system, the instantaneous axis, is always very similar. Rings may be young or old but have definite and characteristic profiles. Moreover, we have found the model to be a robust and realistic dynamical filter.

Synoptic SST analyses for the Gulf Stream region are provided by the NOAA in the form of oceanographic charts primarily based on satellite IR (McHugh and Clark 1984). These charts are useful for a synoptic description of meander location, growth, evolution, and propagation; warm and cold core ring location, propagation, formation; and interaction events. Cloud cover is of course a problem but, since the oceanic time scales are generally slower than the repeat time of the satellite tracks, the picture associated with pieced together sections of fronts available every few days or generally at least every other week can be used to form a picture of the overall synoptic evolution. Cold rings tend to cover over in winter; thus a time series of charts is generally necessary for initialization. Time series of charts can be used for a variety of purposes including initialization, updating, verification, etc. In this study we will simply initialize and verify over a single forecast period to stress the capabilities of the model. The same data could also be used in an assimilation scheme for an ongoing forecast since the model is shown to perform well in the present study.

Figure 3a is a three dimensional schematic in which the stream and ring Feature-Models have been set in place to form an initial condition for the dynamical model. The Gulf Stream Feature-Model uses a thin jet introduced by Niiler and Robinson (1967, hereafter called NR). The across-stream velocity component is identically equal to zero and the along-stream velocity component is written

$$\mu = \exp\left(-\frac{y^2}{g_0^2}\right) V_T \left[\left(1 - \frac{V_B}{V_T}\right)\frac{z}{h_s} + 1\right], \quad z \geq -h_s$$

$$\mu = \exp\left(-\frac{y^2}{g_0^2}\right) V_B, \quad z < -h_s \tag{5}$$

where y is the across-stream coordinate, h_s (=1000 m) is the depth at which $\mu = V_B$ at the stream axis; V_T, V_B are the surface and bottom maximum values of the velocity along the stream axis which have been taken to be 200 and 5 cm s^{-1}, respectively, and g_0 is the horizontal e-folding length chosen to be 40 km. This velocity profile was chosen because it characterizes the position and the average spatial scale of the meanders when the path equation is solved, see NR. The velocity profile for the thin jet Feature-Model is sketched in Fig. 3b. This horizontal structure is fitted on the digitized position of the Gulf Stream axis deduced from the surface thermal fronts shown in the NOAA charts. From the knowledge of the μ field along the stream path, the streamfunction is obtained at each model level by solving the equation $\psi = -\int^y \mu dy'$. Data indicates that the velocity (and temperature) front is sharper on the slope side of the stream than on the Sargasso Sea side. The velocity profile presented here is symmetric across the stream, asymmetry is a possible refinement of this basic Feature-Model and its importance will be a topic of future study.

The Feature-Model used has a transport of 80 Sv (Sv $\equiv 10^6$ m^3 s^{-1}), consistent with various transport measurements across the stream as described in Watts (1983) and Fofonoff and Hall (1983). The vertical shear of the maximum horizontal velocity is 1.95 $\times 10^{-3}$ s^{-1}, in general agreement with the geostrophic shear calculated from an observed horizontal temper-

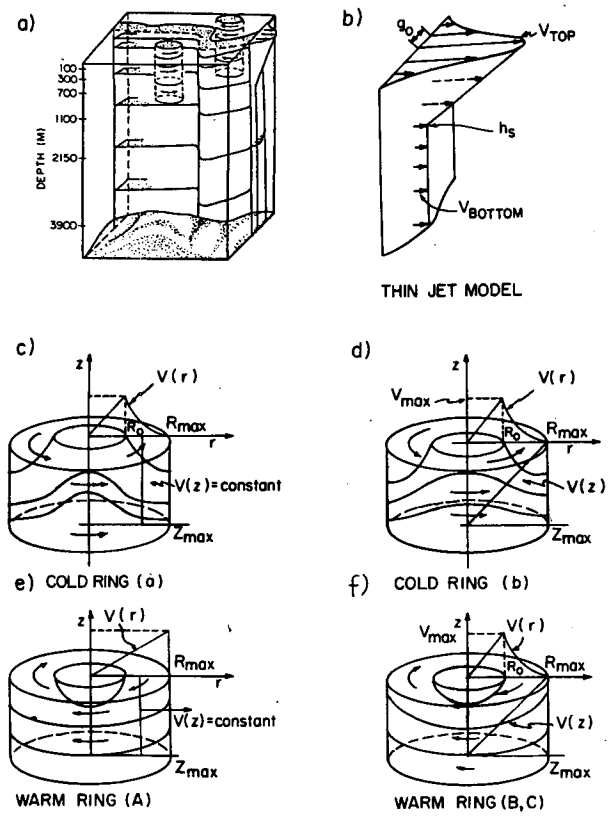

FIG. 3. Feature-Model profiles for Gulf Stream thin jet model: (a) Three dimensional schematic of feature model initialization, (b) along stream velocity profile (μ) as a function of the cross stream coordinate y and of depth (z), (c) horizontal and vertical velocity structure for cold ring model a (see Table 2). r_{max} is the horizontal maximum extension of the ring and v_{max} the maximum velocity reached at r_0. z_{max} is the maximum vertical extension of the ring. (d) Same but for cold ring model b, (e) same but for warm ring model A, (f) same but for warm ring models B and C.

ature gradient of 3°C across 20 km at the midthermocline. A vertical section taken across the thin jet Feature-Model (similar to that shown in Fig. 9b) shows the depth of the 14°C isotherm going from 100 m on the slope side to 600 m on the Sargasso Sea side. This is in close agreement with the jump of 150 ± 50 m to 650 ± 50 m found by Halkin and Rossby (1985). The thin jet model used here is consistent in temperature structure, velocity structure, and transport with available data.

The Feature-Models for the cold and warm rings have been developed with free parameters to best fit the velocity structures of observed rings. In general, we have used a combination of constant, linear, and exponential profiles in the horizontal and/or vertical directions. The ring Feature-Models are characterized by four different parameters: V_{max}, the maximum velocity in the ring; r_{max}, the maximum radius of the ring; r_0, the radial distance at which the maximum velocity is reached; and z_{max}, the maximum depth of the ring. In Figs. 3c–f the profiles used in this paper are schematically represented as a function of these parameters and of the radial distance. The horizontal structure is composed of a linear function up to $r = r_0$ and for $r > r_0$

$$v(r) = V_{max}e^{3(1-r/r_0)}$$

derived from cold ring data by Olson (1980). Warm ring profiles calculated by Joyce (1984) show a similar velocity profile, so this analytic function was used for both the warm and cold ring Feature-Models. The values for the parameters used in the cold and warm ring models are shown in Table 2. These ring models are fit around the geographical position of the center of the rings as seen in the SST maps. The ring velocity fields are inverted to obtain the geostrophic streamfunction solving the Helmholtz equation, $-u_y + v_x = \Delta\psi$. This ring streamfunction field is then superimposed with the thin jet field described above. At the end of this procedure a streamfunction field containing Gulf Stream meanders and rings in appropriate geographical positions is available for initialization purposes, as shown schematically in Fig. 3a. In Fig. 4 we show two different initial ψ fields at 100 m which will be used in the forecast experiments discussed later.

We distinguish three major dynamical processes as the model integrates forward in time: adjustment; interpolation; and evolution. The first and second are associated with the Feature-Model initialization procedure and involve the adjustment of the feature structures and the filling in of the initially zero fields between them. In phase 1, the Feature-Models make slight adjustments over one or two days to satisfy vorticity conservation but their structure remains largely unchanged. During phase 2, an adjustment of the near field occurs as the motionless water adjacent to the stream and rings begins to spin up due to the dynamical interpolation via the quasigeostrophic physics of the model. Interpolation starts immediately and continues to strengthen as the stream and rings evolve. Finally, adjusted and interpolated fields then evolve under mature ring–stream and ring–ring interactions and meandering events as determined by the physics of Eq. (1) subject to the initial and boundary conditions. This phase takes place over time scales of days to weeks and

TABLE 2. Ring model parameters.

Model	Horizontal	Vertical	V_{max}	R_0	R_{max}	z_{max}
		Cold rings				
A	Exponential	Constant	130	60	100	400
F	Exponential	Linear	175	60	100	1000
		Warm rings				
A	Linear	Constant	157	100	100	400
B	Exponential	Linear	157	60	100	1000
C	Exponential	Linear	133	45	70	800

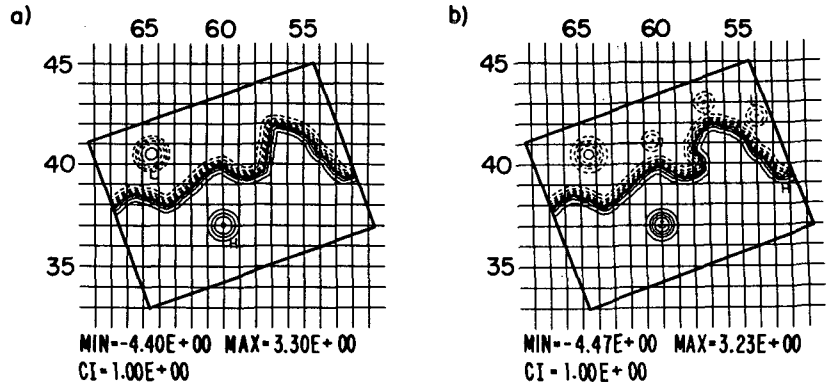

FIG. 4. Initialization geostrophic streamfunction field at 100 m for (a) experiments 1, 2 and 3; (b) experiments 4, 5 and 6.

may result in the formation of new features or the destruction of features present in the initial condition. Evidence of the interpolation phase can be seen in the first few days of a model forecast (e.g., see Fig. 7a). The evolution phase of Fig. 7a will be discussed in detail in section 5.

4. The SST data: 23 November to 19 December 1984

The dataset on which the present study is based consists of the NOAA SST maps for the period of 23 November to 19 December 1984 (McHugh and Clark 1984). In Fig. 5, a temporal sequence of SST maps is

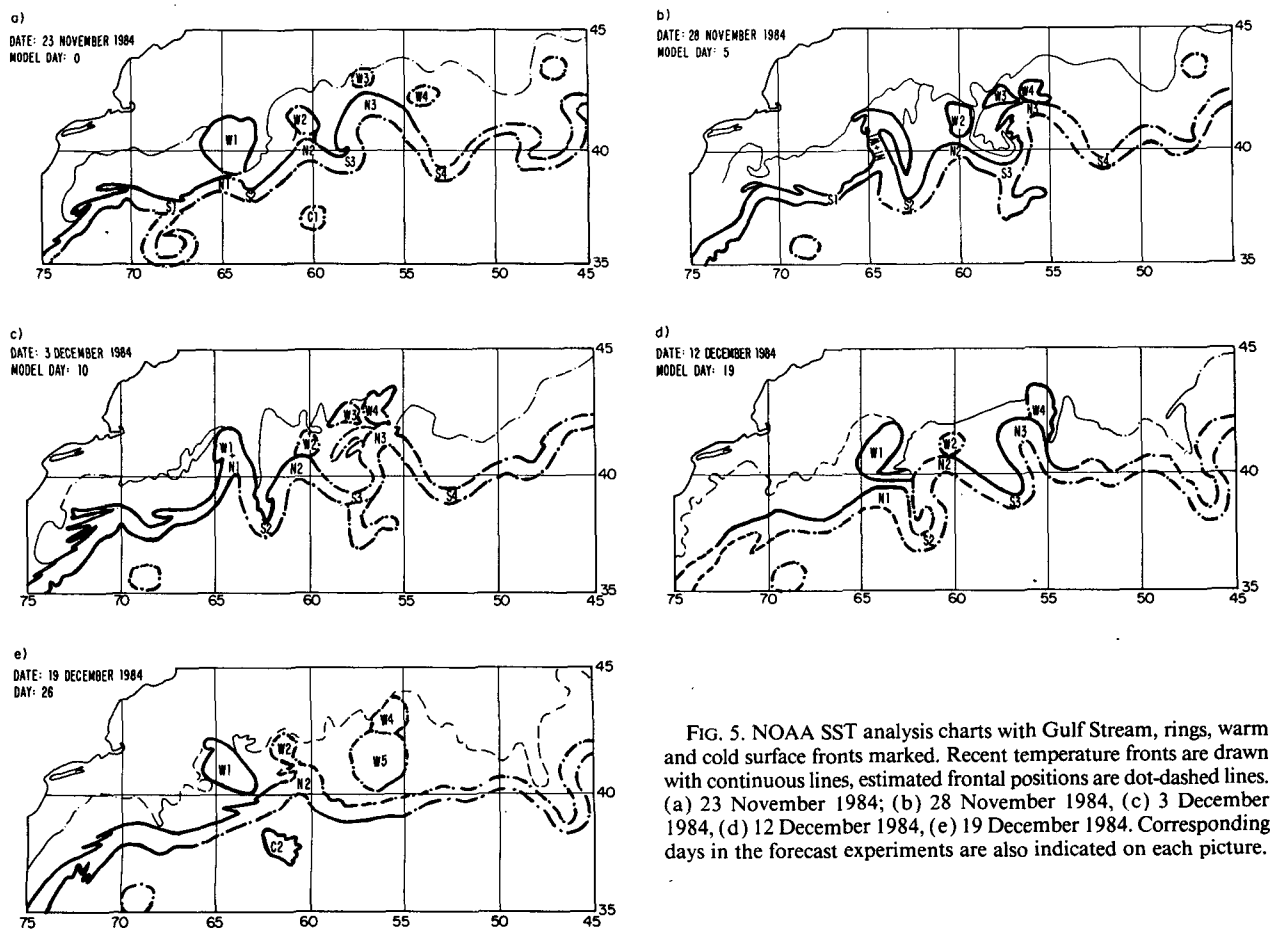

FIG. 5. NOAA SST analysis charts with Gulf Stream, rings, warm and cold surface fronts marked. Recent temperature fronts are drawn with continuous lines, estimated frontal positions are dot-dashed lines. (a) 23 November 1984; (b) 28 November 1984, (c) 3 December 1984, (d) 12 December 1984, (e) 19 December 1984. Corresponding days in the forecast experiments are also indicated on each picture.

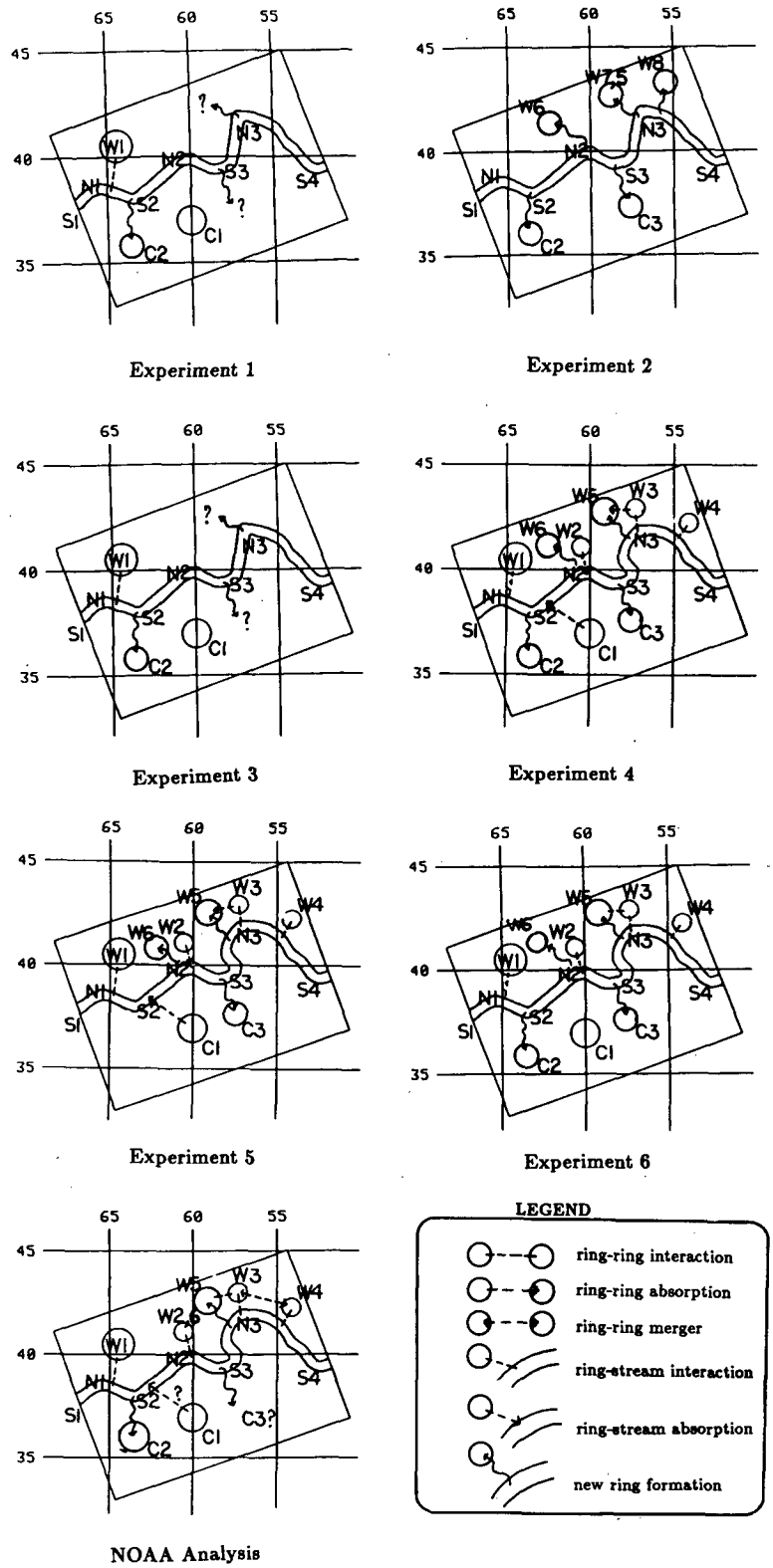

FIG. 6. Schematic of Gulf Stream front position and rings at initialization with indications of interaction, merger, absorption, and ring formation events for each of the six experiments and observations, see legend.

TABLE 3. Summary of major ring events in NOAA analysis and experiments 1–6.

Experiment	C_1	C_2	C_3	W_1	W_2	W_3	W_4	W_5	W_6	W_7	W_8
1	→9	⇒12		→ 5							
2		⇒17	⇒21						⇒16	⇒18	⇒17
3	→9 ←11 →$C_2$12	⇒12 → $C_1$12		→ 5 ←11							
4	→8 ↔19	⇒15	⇒11 →16 ←21	→ 4 ←17	→ 7 ↔11	→2 ←20 ↔ $W_5$20	→ 5 ← 13	⇒20 ↔ $W_3$20	⇒20		
5	→8 ↔16		⇒12 →17 ←20	→ 3 ←19	→ 7 ↔11	→2 ←20 ↔ $W_5$20	→5 ←13	⇒20 ↔W_3	⇒20		
6	→7 ← 13	⇒14	⇒11 →16 ←22	→ 5 ←10	→ 7 ↔10	→2 ↔ 13	→5 ← 12	⇒20	⇒15		
NOAA Analysis	?	⇒17–26	?	→ 5 ←17	→ 7	→$W_4$7 ↔W_4,W_5 19	→ $W_3$7 →7 →$W_5$24	⇒19–24	?		

Notes: →: beginning interaction; ←: end of interaction; ↔: merger; ⇒: new ring formation; ?: questionable or unclear event; Number indicates time of interaction, in model days. Unless otherwise noted, interactions are assumed to be with the Gulf Stream.

selected to display all the new useful data during that period. The thermal fronts are drawn along the Gulf Stream northern and southern boundaries and ring borders. Often visible along the slope side of anticyclonic meanders of the Gulf Stream are thin filaments of Gulf Stream water extending from the crests of meanders into the slope water (e.g., 42°N, 57°W on 28 November); these filaments are referred to as shingles (Stern 1985). The light contours indicate the position of the shelf/slope water front. The continuous heavy lines indicate new data, i.e., clouds were not obscuring the thermal image at the surface. The dot–dashed contouring corresponds to estimated positions of the thermal fronts based on nearby or prior (older than 3 days) data. Surface warming or cooling may be responsible for the nonexistence of a surface thermal signature of a subsurface mesoscale feature of interest and conversely, some surface features may be superficial only. The nomenclature used to label rings and meanders is W for warm (anticyclonic) rings, C for cold (cyclonic) rings, N for northern (anticyclonic) meanders and S for southern (cyclonic) meanders; features are named within our chosen simulation domain only.

On 23 November the stream exhibits a large meander (N_3) located at 42°N, 57°W, surrounded by three warm rings W_2, W_3, W_4 indicated although not observed on this day (Fig. 5a). A larger warm core ring (W_1) is centered near 40°N, 65°W above small anticyclonic (N_1) and cyclonic (S_2) meanders. Examining previous SST maps reveals that data in the area south of S_3, N_3 and S_4 is poor due to upper ocean mixing

TABLE 4. Forecast experiment description.

Run	Duration (days)	Stream position	Cold ring model	Warm ring model	Warm ring position	Model SST	Topography Y/N	Boundary condition
1	13	1†	1a*	1A*	E°	N‡	Y‡	I**
2	26	1	none	none	none	N	Y	I
3	13	1	1a	1A	E	N	N	I
4	26	2	1b	1B, 2C, 3C, 4C	E	Y	Y	I
5	26	2	1b	1B, 2C, 3C, 4C	D	Y	Y	I
6	26	2	1b	1B, 2C, 3C, 4C	E	Y	Y	P

* The letters refer to different horizontal/vertical structure of the rings, see Table 2. The number refers to the ring number as indicated in Fig. 6.

° The letter E indicates that the initial position of W_1 is as shown in Fig. 4, D indicates W_1 is centered 50 km to the south of Fig. 4 position.

† The number 1 indicates the stream axis shown in Fig. 4a, 2 indicates Fig. 4b.

‡ Y and N are abbreviations for yes and no, respectively.

** I and P are abbreviations for interpolated and persisted boundary conditions.

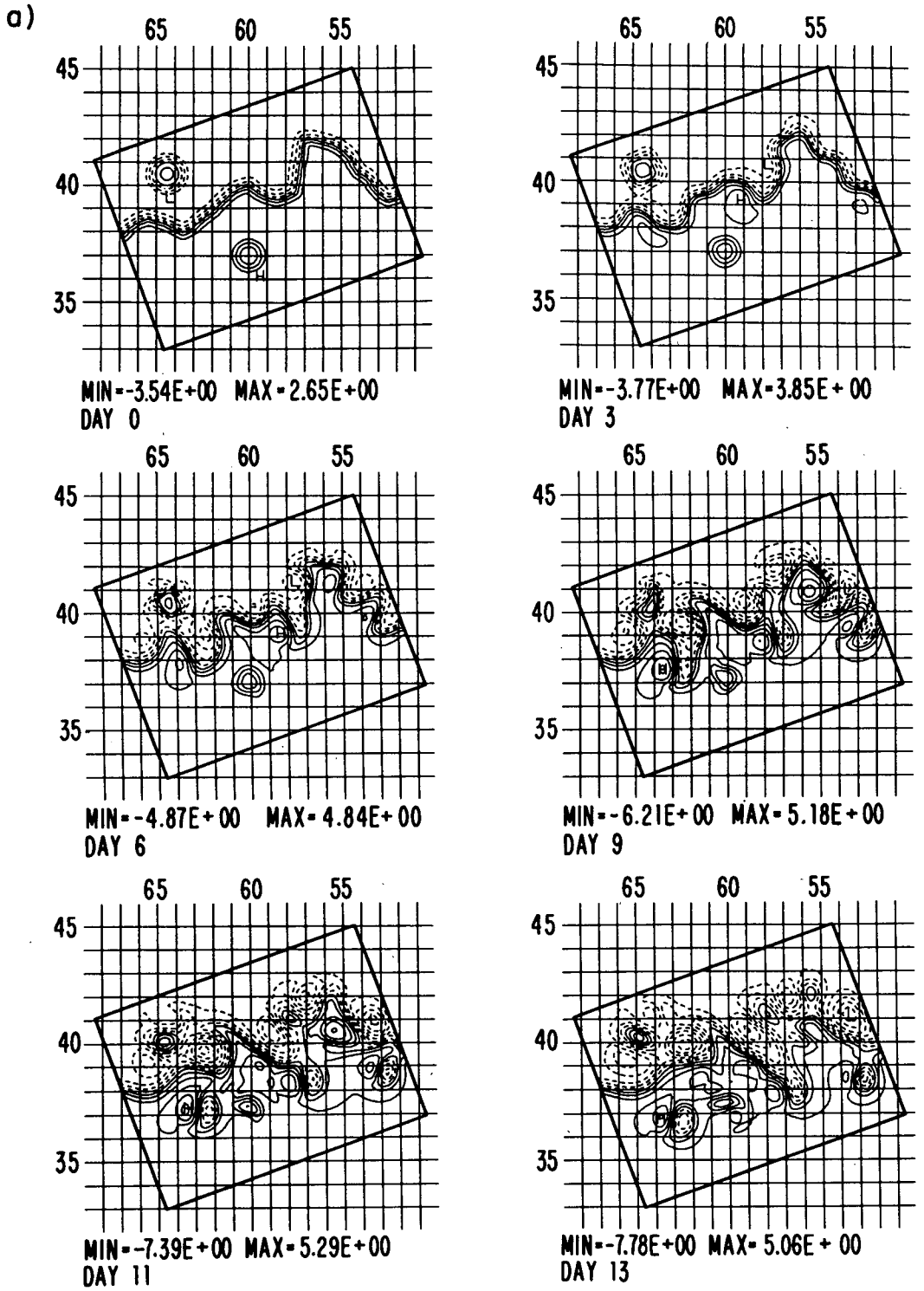

FIG. 7. (a) ψ and (b) q at 300 m for Control-I on selected days, contour interval (nondimensional) is 1.0 for (a) and 6.0 for (b).

and cloud cover for over a month. Moreover, very low temperatures south of S_3 and N_3 indicate the possibility of the presence of cold rings. The cold core ring C_1, is indicated although it has not been observed for 3–4 weeks prior to the period of interest.

After five days the pattern has changed dramatically

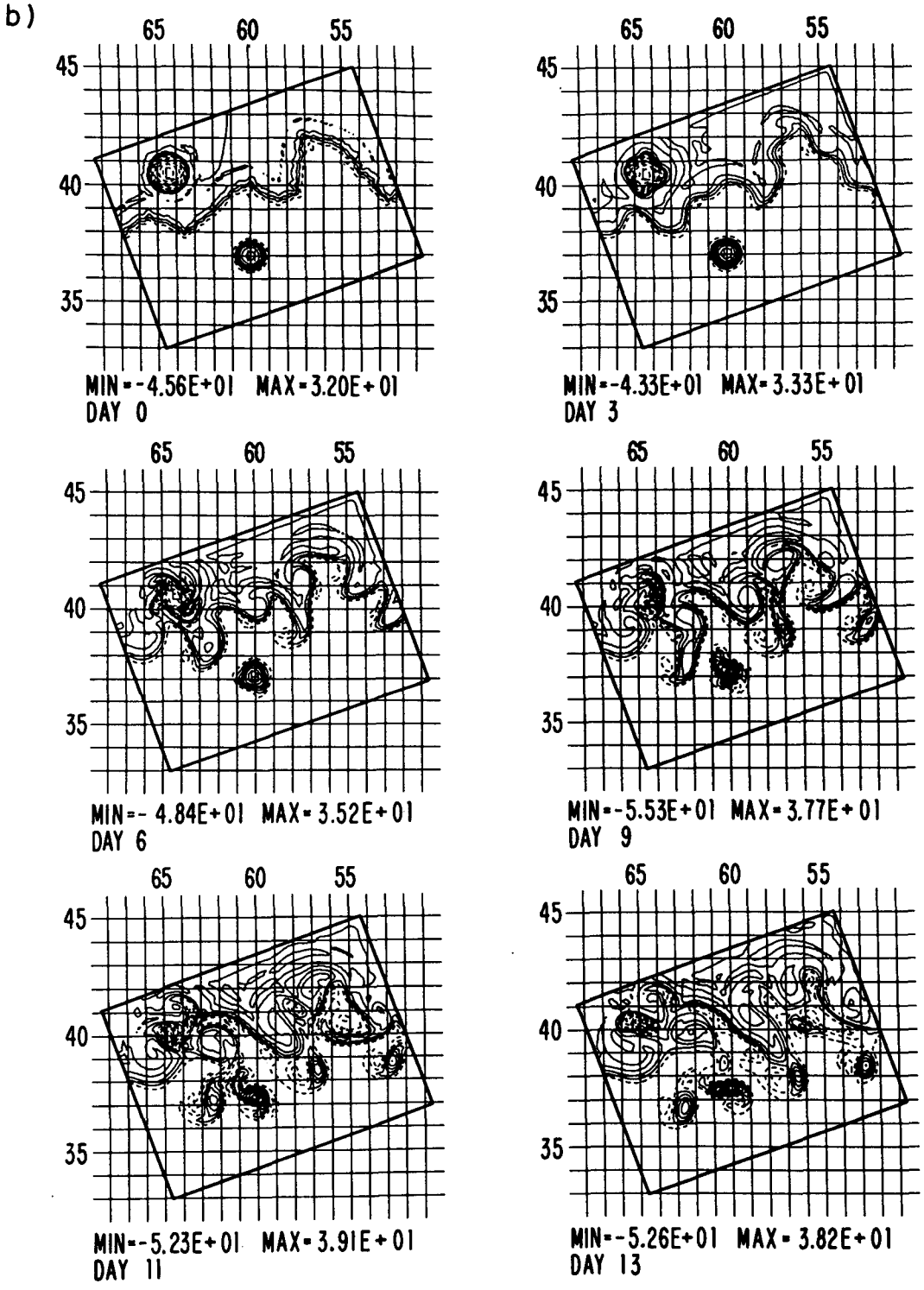

FIG. 7. (*Continued*)

(Fig. 5b). Strong ring–stream interactions and shingling processes are occurring; the rings W_3 and W_4 are observed to be interacting with N_3. The stream is "ragged" to the west of N_3 and a long tiny filament of shelf/slope water seems to be entrained between the rings and S_3. Strong warm ring–stream interaction events are common and it is often difficult to distinguish between the birth of a new warm ring and the attachment

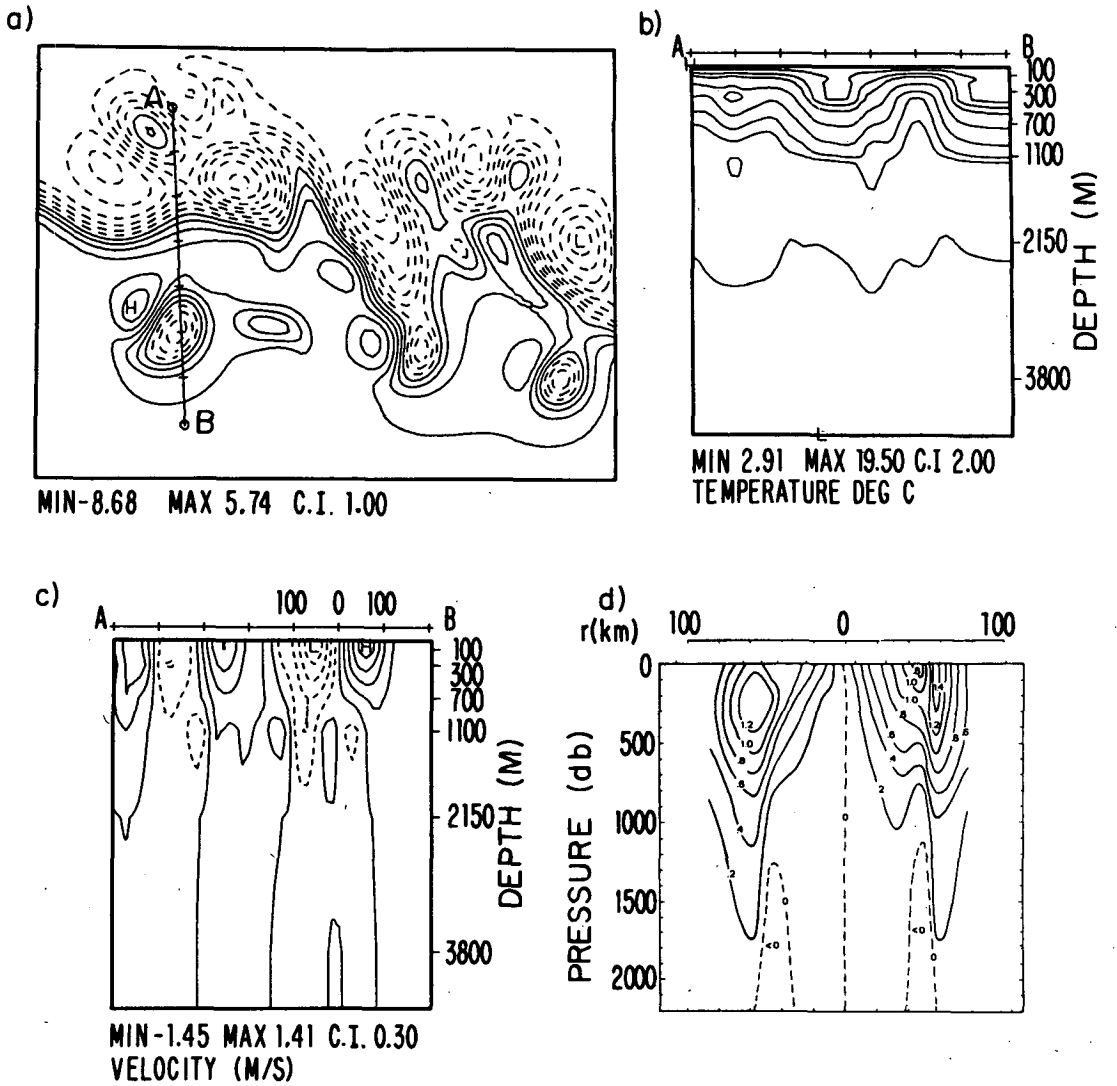

FIG. 8. Cold ring C_2 vertical structure for Control-I. The tick marks along the model cross section A–B indicate 100 km. (a) ψ at 100 m for day 13. (b) Vertical temperature cross section between points A and B shown in (a). (c) Velocity cross section. (d) Observations by Olson (1980) of a cold ring velocity structure.

and successive detachment of preexisting rings. A large warm signal is elongated southward of S_3 as if water was being pulled out of the stream by a cold ring interaction. Around 64° W a visible interaction between the previously distinct warm core, W_1, and the meander N_1 is occurring; the thermal front now extends all the way to the shelf break. At the same time S_2 has increased in magnitude from 5 days earlier. Ring C_1 was eliminated from the chart by NOAA because it had not been observed for 1 month. It is likely that the ring still exists but its position is no longer known.

On 3 December (Fig. 5c), some new data in the western portion of the model domain makes the stream and rings again visible. The trough S_2 has moved further downstream, deepened and narrowed between N_1 and N_2. Ring W_1 is still attached to the stream and interacting strongly. No new data was available in the eastern region near 57°W where, twelve days earlier, strong ring–stream interactions were occurring.

The next two pictures (Figs. 5d, e) display the evolution of N_3 and S_2, which results in the formation of two new rings. A new warm core ring, W_5, was formed between 12 and 17 December, in model days 19–23; a new cold core ring, C_2, was formed between 10 and 19 December, in model days 16–25. In both cases the formation was preceded by strong warm core–stream interaction events, meandering of the northern front of the stream and possibly an injection of Gulf Stream water to the Sargasso Sea from S_3. Furthermore Fig. 5e shows W_4 interacting with W_5 forming a rare but characteristic "attached ring couple."

Figure 6 and Table 3, discussed further below, in-

clude schematics and times of occurrence of the major features and events in the NOAA analysis described here. In Fig. 6, a ring in the vicinity of 60°W is labeled $W_{2,6}$ because several experiments absorb W_2 and replace it with a new ring W_6 during a period of cloud cover.

5. Gulf Stream simulations

a. Forecast experiments

Here we describe a set of numerical experiments that predict the position of the Gulf Stream front and rings starting from simulated 23 November 1984 initial-boundary conditions based on the data of section 4. The objectives of these experiments are: (i) to study basic processes of meander evolution and ring production; and (ii) to test the ability of our present scheme (model and methodology) to simulate realistically the total flow system over a several week period. Table 4 characterizes six forecast experiments in which different initial conditions were chosen for the starting number, structure, and position of the rings and of the Gulf Stream front. The standard model parameters used in these experiments are displayed in Table 1. Experiments 1 and 4 are the control experiments (called Control-I and Control-II, respectively); their initial streamfunction fields are shown in Fig. 4. Control-I is also the control experiment for the cold ring formation process studies and model sensitivity experiments of section 6a. In the initial condition for Experiment 1 only two rings, W_1 and C_1, are present and the Gulf Stream axis position along N_3 is relatively sharply peaked. We regard Control-II as our best initial streamfunction estimate. All the rings are present with improved structure models and the rounder shape of the N_3 meander is closer to the observations. For experiments 1–5 the boundary conditions for streamfunction and vorticity are obtained by a linear interpolation of the inflow and outflow positions of the thin jet between the data days of Fig. 5. Experiment 6 uses boundary conditions persisted from the initial conditions.

Shown in Fig. 6 is a schematic map of each of the six forecast experiments including the initial Gulf Stream position and initial and final ring positions and indications of ring interaction events such as contacts, mergers, absorptions, and formations, etc. These schematics are useful for keeping track of the qualitative behavior of each of the forecasts in relation to that observed in the IR data. Questionable or unclear events are indicated by a question mark. A summary of these events can be found in Table 3.

1) EXPERIMENT 1: TWO RING; CONTROL-I

The 300 m streamfunction field for forecast experiment 1 is shown in Fig. 7a. Only rings W_1 and C_1 are present in the initial condition. Although not clearly evident here, phase 1 of the adjustment process makes small adjustments to the features between day 0 and day 3. Phase 2 is visible on day 3, weak anticyclonic eddies have begun to spin up adjacent to the stream on the Sargasso Sea side. As the dynamical evolution takes place, these near fields are seen to grow and develop, closely coupled to the shape of the meandering stream. From day 3 to 13, phase 3, the evolution process shows some major dynamical events taking place. On day 6 the warm ring–stream interaction (W_1–N_1) and deepening meander (S_2) from 62° to 64°W begin to develop. By day 9 the interaction is very strong and the meander has more than doubled in magnitude since day 0. The interaction weakens again by day 11 and the deep "sock" meander has just about pinched off a new cold ring at 37.5°N, 62.5°W. Day 13 shows the new cold ring clearly separated from the stream, the warm ring is no longer interacting with the stream, and the Gulf Stream has gone back to a smooth, strong, coherent jet. The original cold ring C_1 lost much of its strength to the stream during its interaction. East of 60°W adjustment processes develop near field eddies along both sides of the stream. The meandering jet appears to be forming small, ringlike features (38.5°N, 56.5°W and 41°N, 58°W day 11 and 42°N, 55.5°W on day 13) but they do not escape from the jet. It is important for the interpretation of this and similar pictures to remember that the Gulf Stream axis runs along the line of maximum downstream velocity, not along the zero contour of the streamfunction, which at first catches the eye.

The 300 m vorticity field, q, for Experiment 1 is shown in Fig. 7b. Notice the small scale variability present in the initial condition has been filtered out by day 3, this is phase 1 of the adjustment process. The ring–stream interaction and deepening meander are visible on days 6 and 9. Filamenting vorticity from the tip of the meander is wrapping around the near field eddy on days 9 and 11. The new cold ring C_2 is evident as a large patch of positive vorticity at 36.5°N, 62.5°W on day 13. The vertical structure of the ring and nearby fields is illustrated in Fig. 8 and is discussed in section 5b.

The thermocline and deep flow is shown in Fig. 9. At a depth of 700 m (Fig. 9a) the flow undergoes the same kind of dynamical adjustments as occur at 300 m near-field eddies are visible all along the meandering stream on day 6. Although W_1 was not present in the initial pressure field, by day 9 the vertical and horizontal nonlinear interactions have produced a small warm core below the upper level ring. Apparently the initial structure of W_1 was not deep enough and the model adjusted the deep flow for compatibility with the upper level velocity fields. The signature of the deep sock meander and the formation of C_2 is evident. The near-field eddy shows as strong a pressure signature as in the newly formed ring, 37.5°N, 63.5°W on day 11. Figure 9b shows the signature of this dipole also at

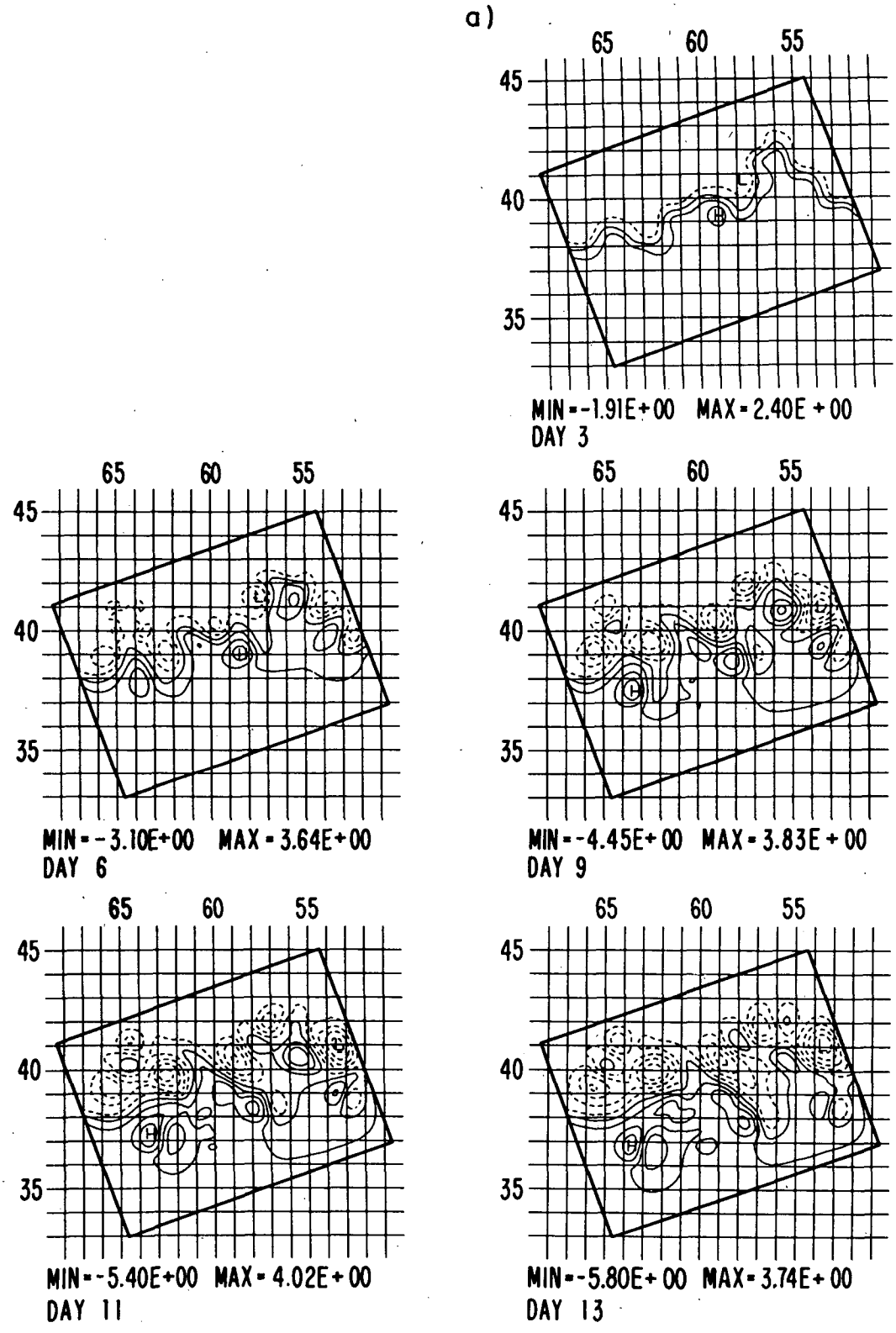

FIG. 9. ψ at (a) 700 m (b) 2150 m for Control-I on selected days, contour interval (nondimensional) is 1.0 for (a) and 0.5 for (b).

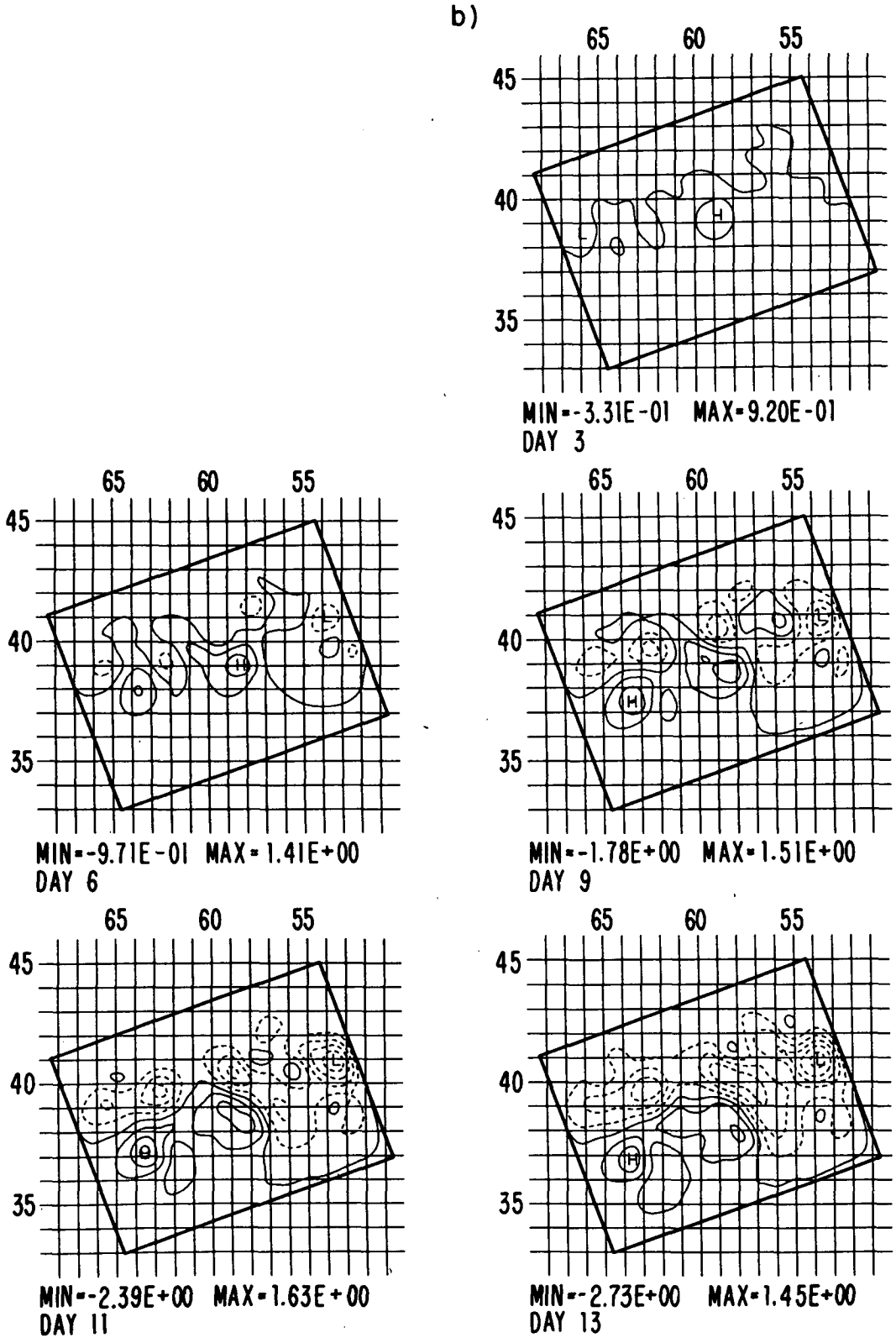

FIG. 9. (*Continued*)

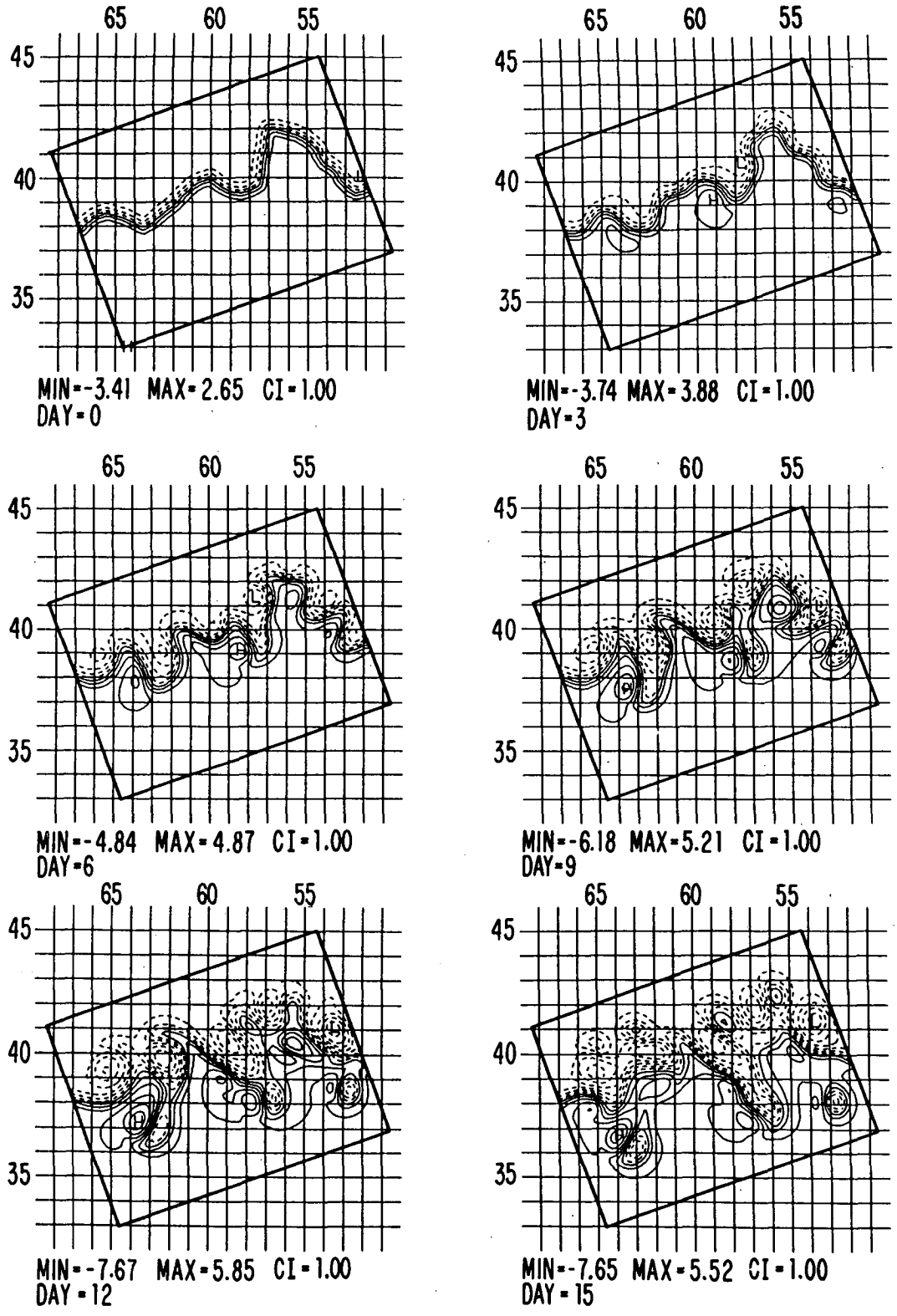

FIG. 10. ψ at 300 m for experiment 2 on selected days. Contour interval (nondimensional) is 1.0.

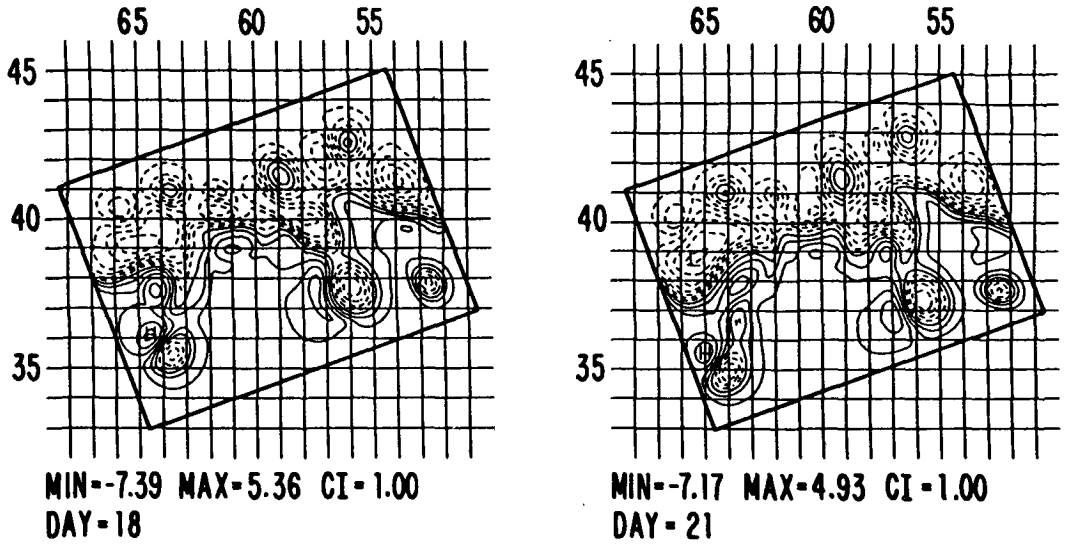

FIG. 10. (*Continued*)

2150 m, indicating that the near-field anticyclonic eddy has a strong pressure signature in the deep flow and that an important component is barotropic. At this deep level, the stream axis is not clearly defined throughout the domain and the field is populated by large eddies around which the deep Gulf Stream transport filaments and intrudes up and down the bottom slope. The near-field eddies have a strong bottom signature that can mask the relatively weak deep current underneath the high velocity core of the surface Gulf Stream.

2) EXPERIMENT 2: NO RINGS-I

In experiment 2 the rings W_1 and C_1 were removed from the initial condition used in the control experiment. Figure 10 shows the 300 m streamfunction at selected days of a 26-day forecast. Initial adjustment of the stream and development of the near-field eddies is very similar to that of the control experiment. On day 9 slight differences are evident in the shape of the deep sock meander. It appears that the meander will pinch off the new cold ring cleanly, day 12, but the forecast shows that, although the ring has pinched off, even by day 21 the ring is not completely free of the stream in the pressure field. The shape of the deepening meander, the time of ring formation, and the shape of the newly formed ring are all affected by the presence of rings adjacent to the stream in the initial condition. The eastern half of the basin looks very similar to that of the control experiment on day 12. The absence of W_1 and C_1 seems to have only local effects for at least the first two weeks of integration. This run shows that the two small ringlike features also found in Control-I (at 41°N, 58°W and 42°N, 55.5°W) evolve into large rings which locate themselves where W_5 and W_3 are observed in the IR data. In fact, by day 21, three new warm rings have been formed in the region where the observations show four rings, three evolved from the initial condition and one was newly formed. Here the model has produced new rings where they were incorrectly missing in the initial condition. The new ring positioned where W_5 is observed is labeled $W_{7,5}$ in Fig. 6 because its formation process appears to be different than that observed in the gappy SST data.

3) EXPERIMENT 3: NO TOPOGRAPHY-I

In experiment 3 we initialized the model with the same initial streamfunction and vorticity fields as in experiment 1 but with no topography. The initial adjustment processes are virtually the same for both experiments. The evolution of the stream, ring–stream interactions, and the birth of the new cold ring are all reproduced without bottom topography. There are slight differences in the pressure field on day 13 but the features and Gulf Stream front position are qualitatively the same. Because the results are so similar, they have not been presented here.

4) EXPERIMENT 4: REALISTIC SIMULATION; CONTROL-II

Control-II uses the best estimate of the Gulf Stream and rings for model initialization. Three additional warm rings have been placed in the eastern part of the domain at the estimated positions given in the satellite data. The depth and velocity structure has been made more realistic in each of the ring models. Each of the rings has been sheared in the vertical, and an exponential decay in velocity has been added to the outer edge of the warm core rings; see Table 2 and Fig. 3.

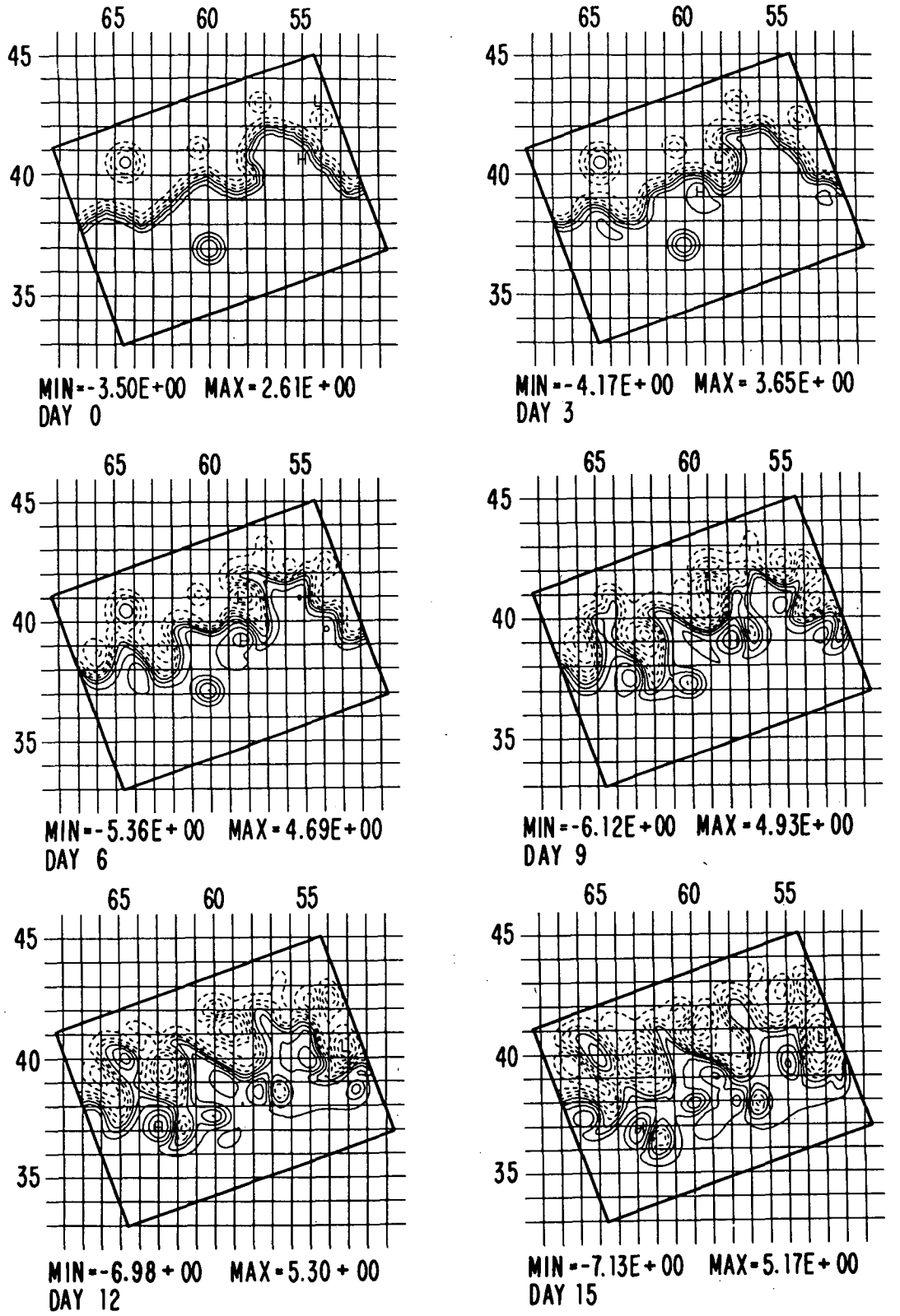

FIG. 11. ψ at 300 m for Control-II on selected days. Contour interval (nondimensional) is 1.0.

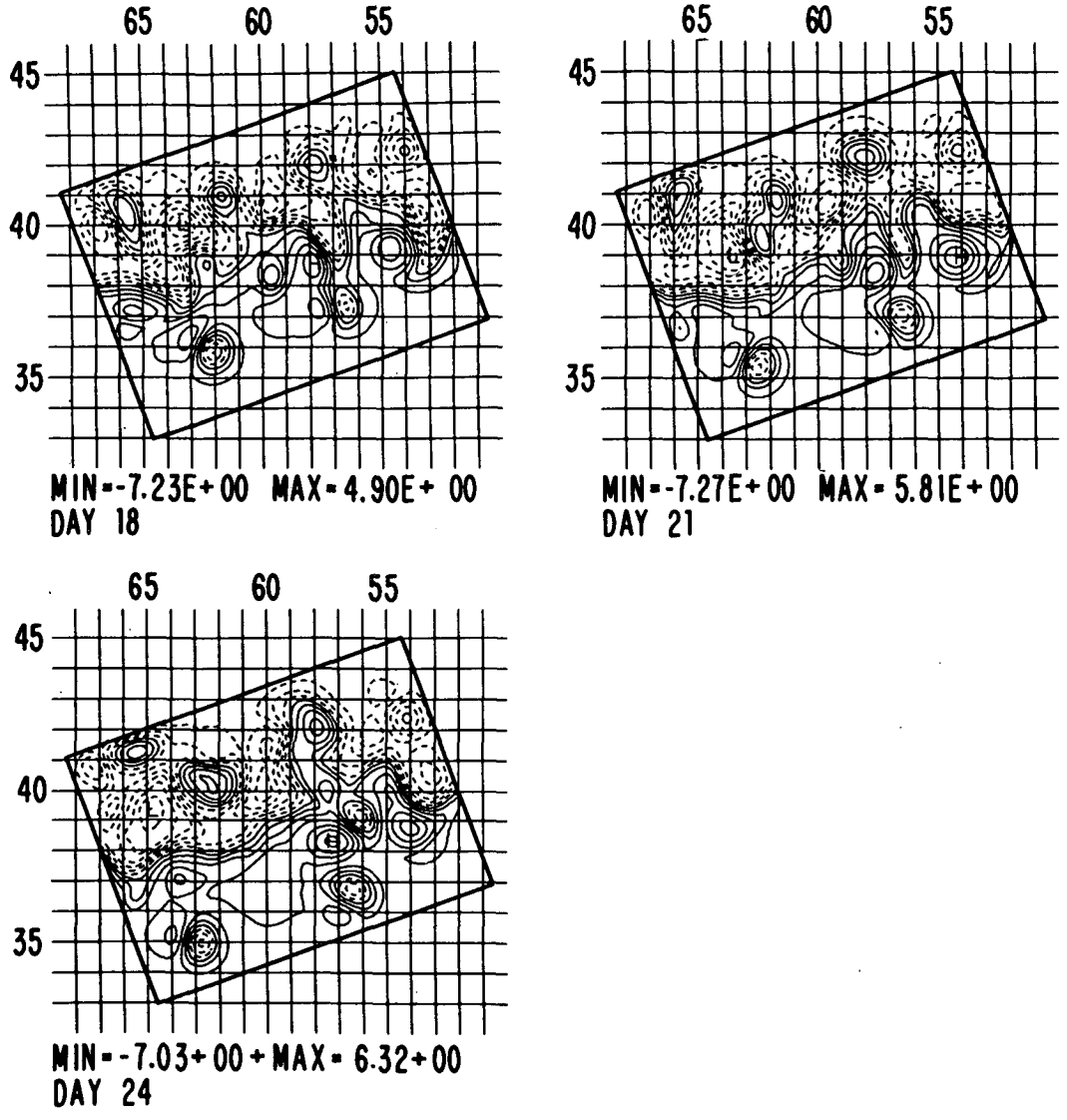

FIG. 11. (*Continued*)

The shape of the Gulf Stream is more consistent with the observations near 58°–56°W. This model run was also initialized with a variable top density.

The 300 m streamfunction for this experiment is shown in Fig. 11. The initial stages of adjustment are quite similar to Control-I. The near-field eddies, which develop during phase 2, are about the same strength and in the same locations as those seen in the previous exercises. However there is one major difference between the Feature–Model adjustments: in experiment 1, W_1 becomes very distorted, it is almost square in shape on day 6 (see Fig. 7b), while in experiment 4 the ring remains smooth and round during this phase even though the level of interaction with the stream is nearly the same between the two cases. It appears that the unrealistic velocity structure used for experiments 1 and 3 caused oscillations to develop along the border of the warm ring. Similar behavior is seen for ring C_1 although it is not as pronounced.

Evolution of the flow field (phase 3) in the western portion of the basin is similar to that of Control-I but shows some interesting differences. The ring–stream interaction W_1–N_1 is very strong on day 9, the pressure fields of the ring and stream appear to have merged. During this phase the interaction of W_1 with the stream is very different from Control-I. Day 12 shows W_1 re-emerging from the stream, C_1 is interacting with the deep sock meander, and the pressure contours are beginning to pinch off to form the new cold ring. The newly formed cold ring and near-field eddy are moving to the southwest on day 15, several days later than the formation in Control-I. Warm ring W_1 separates from

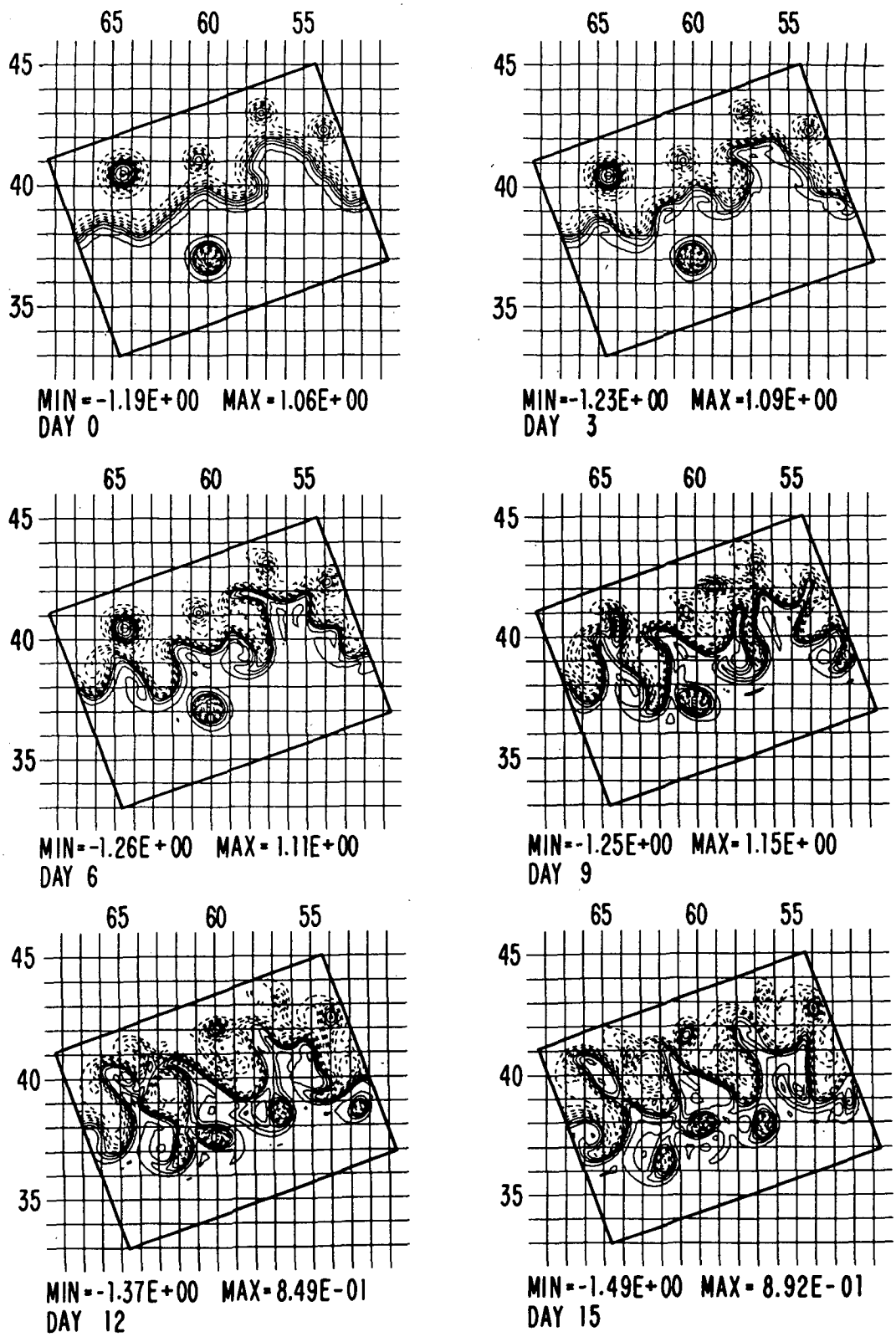

FIG. 12. Geostrophic surface density anomaly ψ_z for Control-II on selected days. Contour interval (nondimensional) is 0.2.

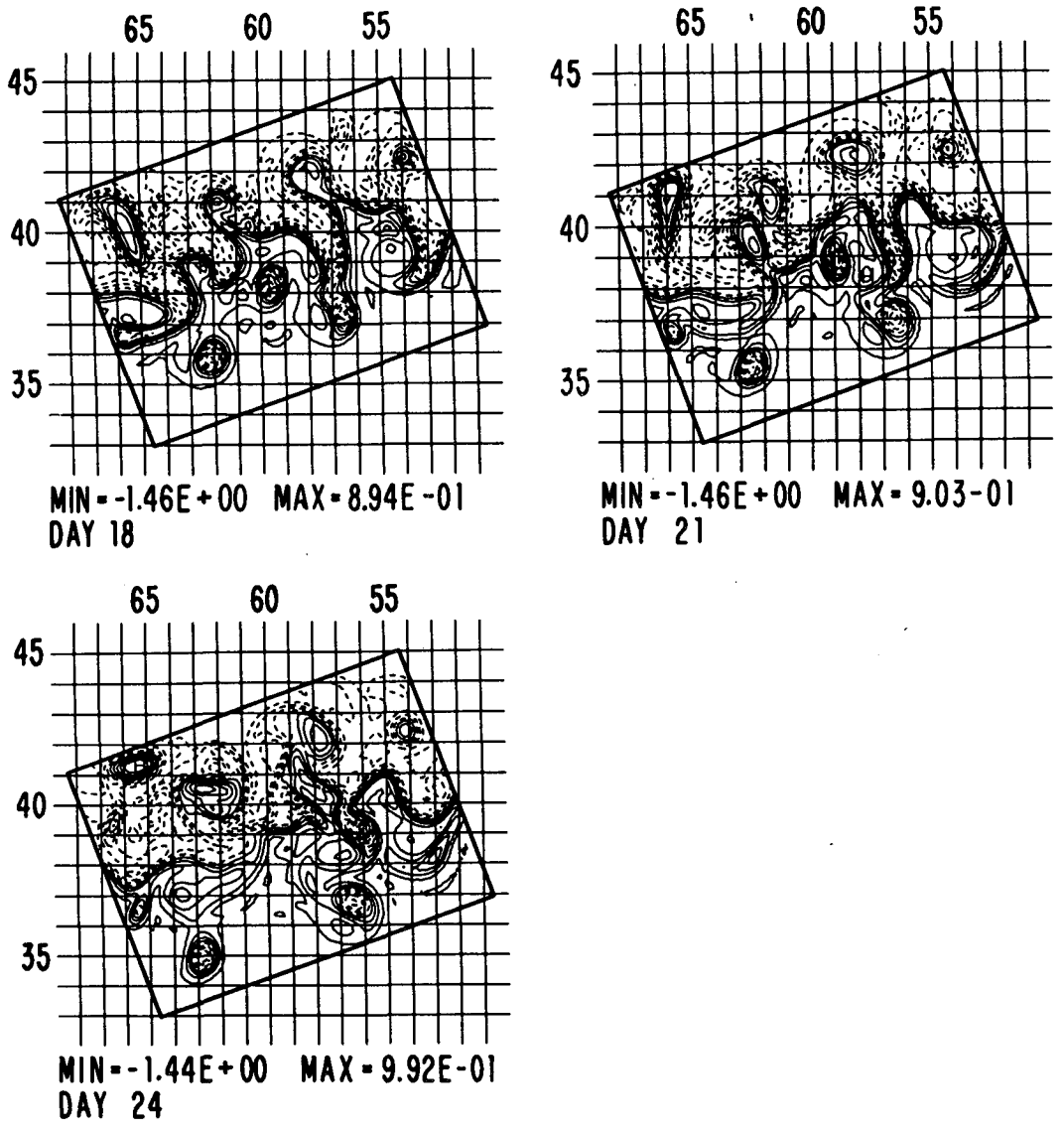

FIG. 12. (*Continued*)

the stream and moves off to the northwest where it interacts with the continental shelf.

The eastern portion of the basin behaves quite differently with the modified stream position and the addition of three warm rings. On day 6 a shingle-like filament of Gulf Stream water is being injected into the slope water, a small patch is visible at 42.1°N, 59°W on day 9. With the exception of the shingle, the Gulf Stream front looks very similar to Control-I. However, on day 12 a large bump starts to grow out of the side of the meander at 41°N, 57°W. This perturbation continues to develop until on day 18 the pressure contours begin to cut off to form a new warm ring, W_5. The cutoff is complete on day 20, day 21 shows W_5 separated from the stream and by day 24 it has begun to interact strongly with the stream.

Warm rings W_2, W_3 and W_4 present in the initial condition undergo many interactions with the stream and other rings. Ring W_2 interacts and is absorbed by meander N_2 which then spawns a new warm ring, W_6. Ring W_3 interacts with the developing meander at 42.5°N, 57°W and is eventually absorbed by the newly formed W_5. Ring W_4 interacts with the stream early, days 6–9, and reemerges stronger than it was initially.

To conclude, experiment 4 was initialized with realistic Feature–Models consistent with the observed data. The W_1–N_1 interaction, deepening of S_2, and the birth of the new ring C_2 are all reproduced well. In the eastern portion of the domain shingling activity preceded the meander growth and birth of a new warm ring, W_5. Several of the initial rings interacted with the stream and with each other, their fates included both

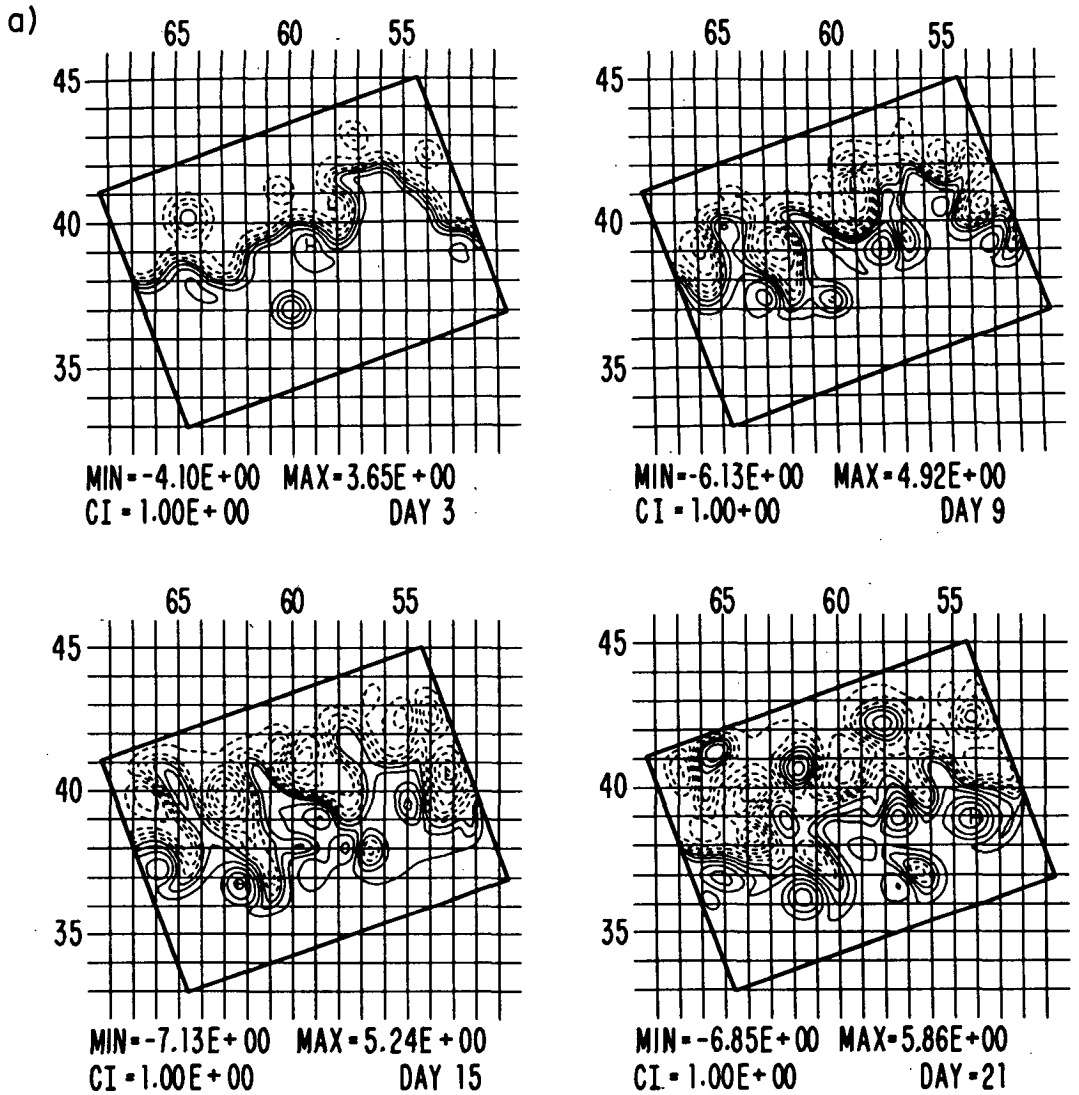

FIG. 13. (a) ψ field for experiment 5 at 300 m. (b) ψ field for experiment 6 at 300 m.

absorption and survival. The final state is in agreement with the observations on the number and in general agreement with the position of rings in the model domain. The final position of the stream is in good agreement with the observations from the inflow at 67°W to about 57°W. East of that point the partial IR data does not confirm or contradict the small double meander predicted by the model. A discussion of the surface density features, Fig. 12, is given in section 5b.

5) EXPERIMENT 5: INTERACTIVE WARM RING-II

The difference between the initial condition for this experiment and experiment 4 is that W_1 was placed closer to the stream. The IR surface signature of W_1 is of larger extent than the subsurface structure of W_1 could reasonably be expected to be, so this sensitivity is explored. Early development is similar for the two experiments, and the fields on day 9 are almost identical. However, on day 15 we can see from Fig. 13a that W_1 is still strongly interacting with the stream and the deep sock meander is being advected to the east. The birth of C_2 is in fact completely inhibited by the prolonged interaction between W_1 and N_1. Here the position of a preexisting ring near the stream has a controlling effect on ring formation.

6) EXPERIMENT 6: PERSISTED BOUNDARY CONDITIONS-II

In this experiment, the same initial conditions were used as in experiment 4 but the boundary conditions were held fixed rather than being interpolated from Fig. 5a–e. Originally designed to evaluate persisted

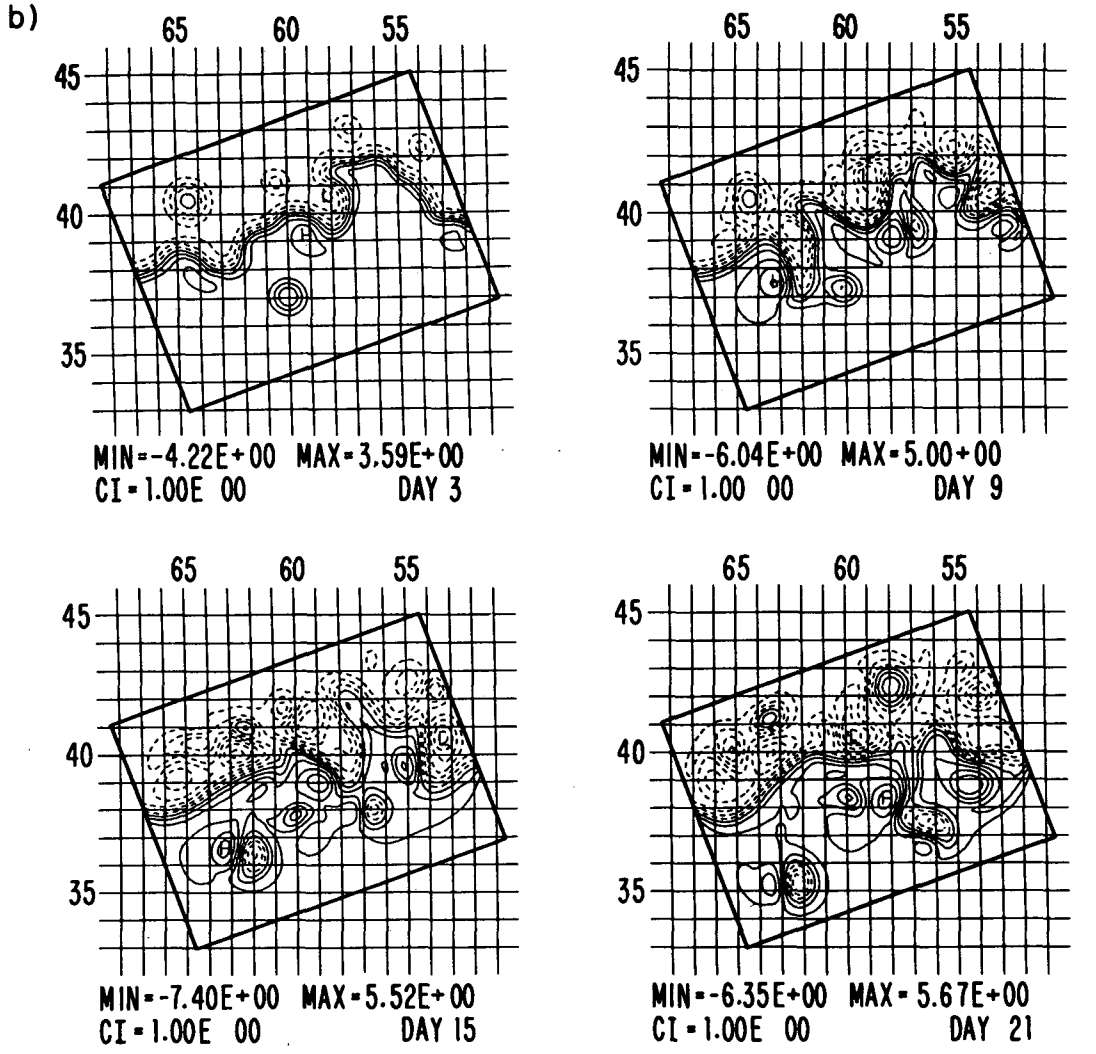

FIG. 13. (*Continued*)

boundary conditions, this experiment also imposes a smoother inlet flow since during this period the interpolated boundary condition oscillates the direction of the stream.

The 300 m streamfunction field for experiment 6 is shown in Fig. 13b. Initial developments were very similar to the Control-II experiment. On day 9 however, the W_1–N_1 interaction is much weaker. The development of the deep sock meander appears to be uninhibited and a slightly stronger C_2 forms in nearly the same time and place as in experiment 4. The major difference is in the shape and strength of the Gulf Stream on day 15. Because the inflow is straight and the W_1–N_1 interaction is weaker, the Gulf Stream remains very smooth and strong from 60° to 67°W after ring formation. Ring W_1 was weakened considerably from its interaction with the stream where in experiments 4 and 1 it reemerged stronger after the interaction.

b. Discussion

Control-I was our first attempt to model the cold ring formation observed in satellite IR between 23 November and 19 December 1984. The Feature–Model initialization procedure and quasi-geostrophic dynamics produced some realistic results. Ring W_1 was initialized adjacent to the stream but, as was seen in the

TABLE 5. Sensitivity experiments and parameter values.

Run		α	β	Γ^2
Control-I	a	3.5	0.25	1.4
nonlinear	b	10.5	0.25	1.4
linear	c	1.1	0.25	1.4
thermal	d	3.5	0.25	4.2
relative	e	3.5	0.25	0.46
linear beta	f	1.1	2.5	1.4
beta	g	3.5	2.5	1.4

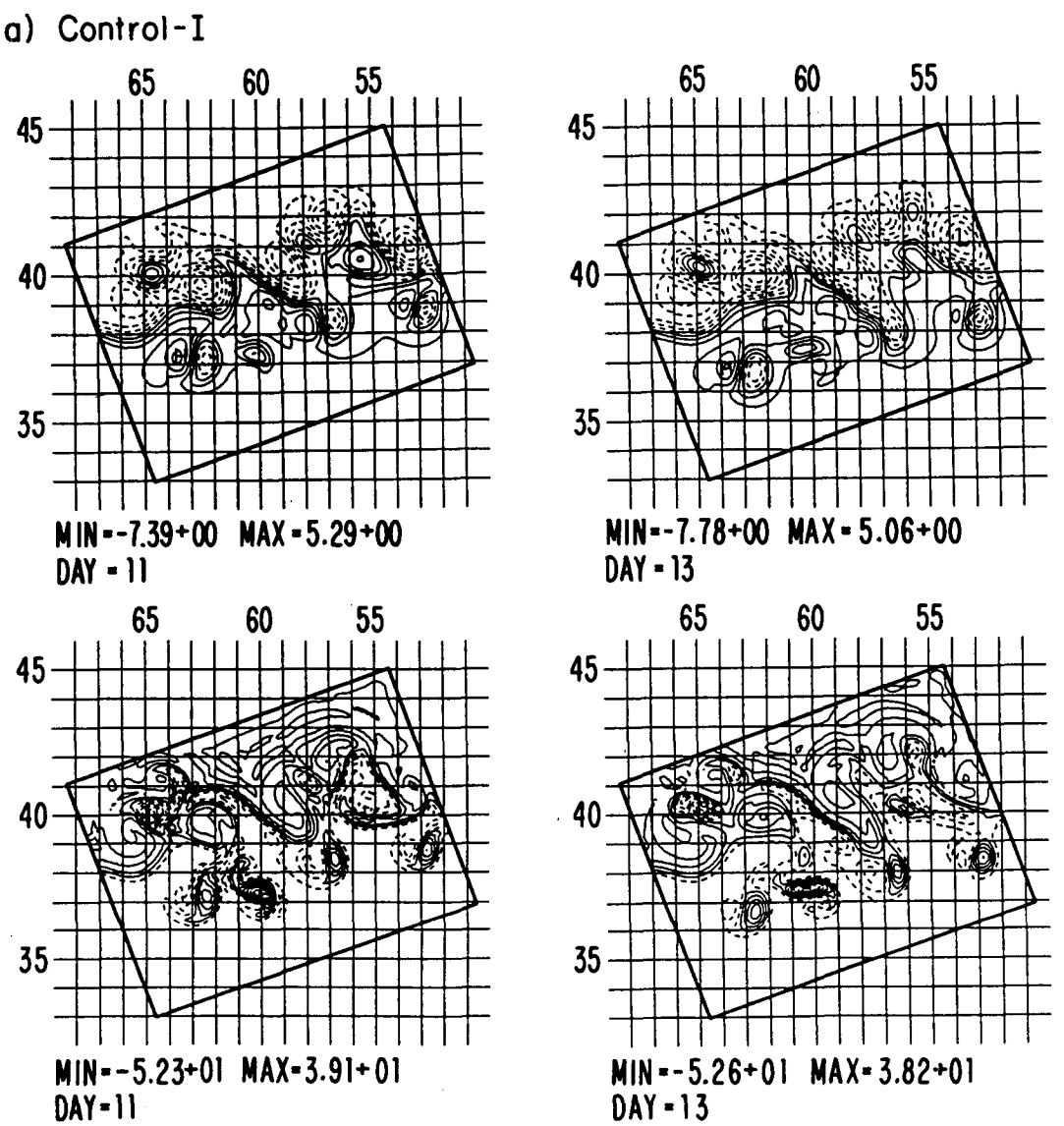

FIG. 14. Parameter sensitivity experiments ψ (upper) and Q (lower) on days 11 and 13 for (a) Control-I, (b) nonlinear, (c) linear, (d) thermal, (e) relative. Nondimensional contour intervals are 1.0 for ψ and 6.0 for Q.

IR, soon interacted strongly with meander N_1. Just downstream of this interaction, a deep sock meander developed and spawned a new cold ring. The time of formation in the model experiment was 12 days, compared to 17–26 days in the IR observations. Although the model ring formed a little fast, its location and size are very similar to the observed ring. Vertical sections taken through the new ring show that the velocity structure is in excellent agreement with the velocity profile of ring BOB, Fig. 8 (Olson 1980). The model ring has even developed deep countercurrents as seen in the data (the level of no motion used by Olson was 2500 m). Ring BOB was formed in 1977 at about the same latitude as our model ring but a little farther to the west, near 69°W. The temperature section in Fig. 8b also clearly shows the classical dome of the isotherms in the cold ring.

During the first 9 days of the model forecast, intermediate scale waves grow on the larger scale meandering pattern of the Gulf Stream; they are most visible in the eastern portion of the domain on day 6. We feel that these waves grow as a result of the initial equilibration process between the Gulf Stream and the surrounding motionless waters. The near-field eddies seem to have a stabilizing effect on the growth of these waves because none are seen to develop after the interpolation phase of the adjustment process is complete. Note that this meander scale corresponds to the most unstable temporally growing normal mode of the linearized eigenvalue problem for an eastward flowing thin jet,

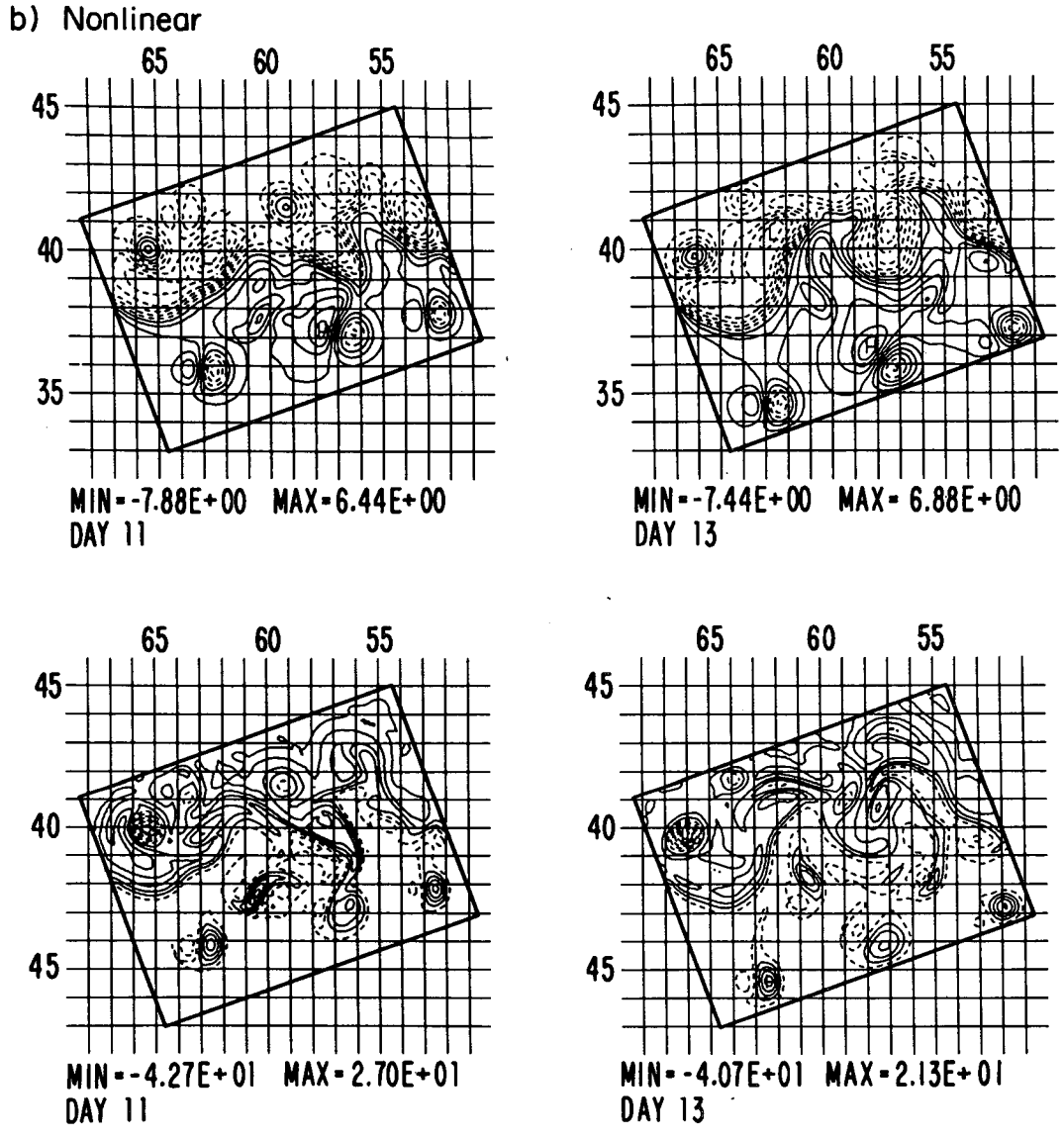

FIG. 14. (*Continued*)

λ = 280 km (Holland and Haidvogel 1980). Subsequent tuning of the Feature–Model parameters and the numerical technique used to digitize the stream axis has been found to reduce the growth of these intermediate scale waves; large scale evolution and major dynamical events are unaffected, so the results are not included in this study.

The three phase evolution process gives rise to near-field eddies adjacent to the stream. Ikeda and Apel (1981) found somewhat similar eddies studying the spatial growth of disturbances in an eastward flowing jet, which developed into "basin scale" secondary circulations. Our anticyclonic near-field eddies are associated with a local meander intensification and have a scale comparable to the area of the deepening meander. They are also seen to move away from the stream and decrease in strength during ring formation events. The cyclonic near-field eddies north of the stream are not always associated with meanders but generally fill up the region between the stream and rings. This north–south asymmetry in the near-field adjustment may be related to the initial shape of the Gulf Stream front, initial position of the rings, and the continental shelf, modeled as a solid wall.

Experiments 2 and 3 were designed to test the sensitivity of the initial adjustment phases and the ring formation process to the presence of nearby rings and bottom topography. In both cases the initial adjustment and interpolation are essentially the same as in the Control-I experiment. However, while the evolution phase in the absence of rings still produces a new cold ring, its time of formation, size, and structure are dif-

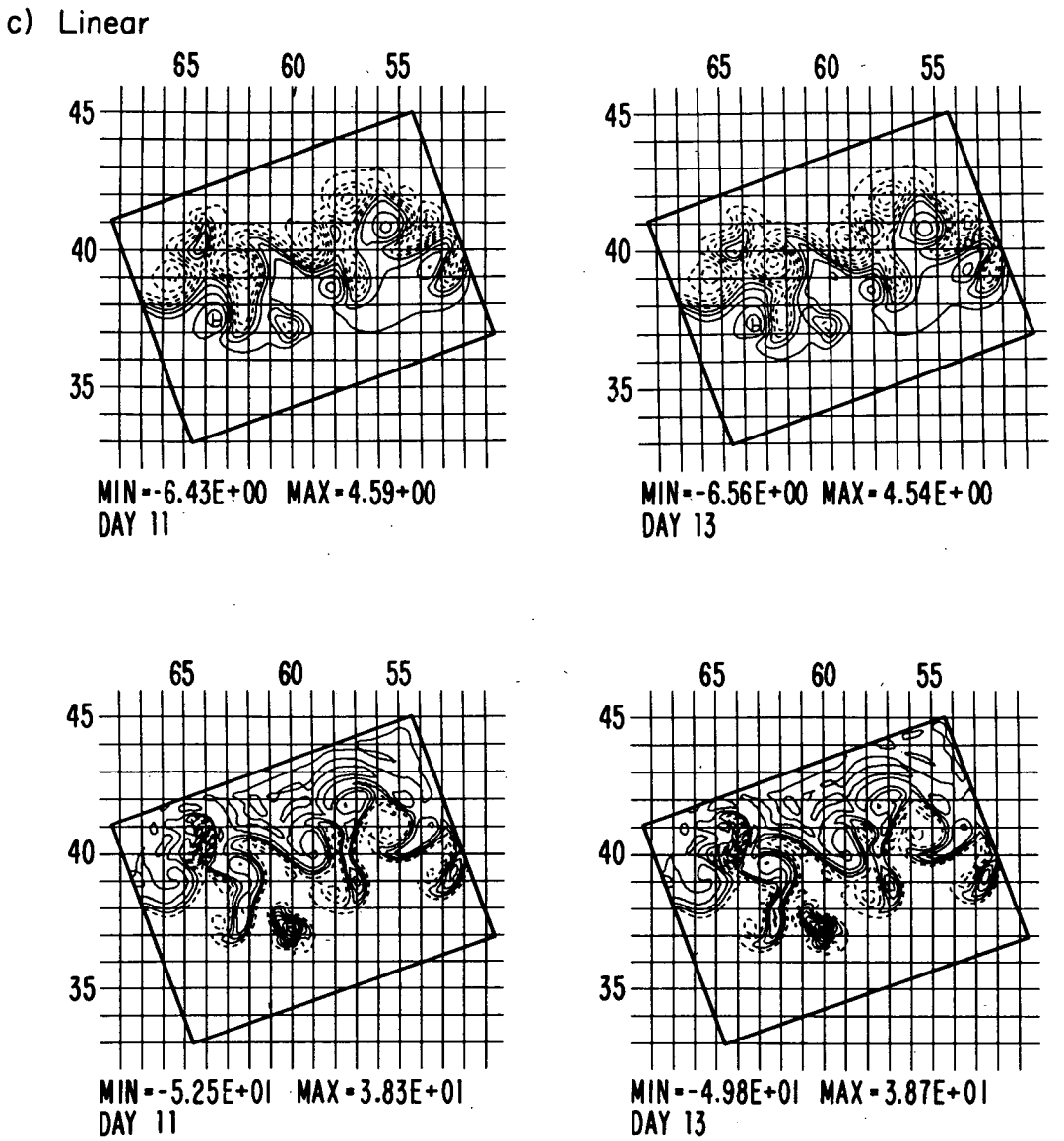

FIG. 14. (*Continued*)

ferent. The ring–stream interaction prior to the formation of the new cold ring does not significantly affect the development of the deep sock meander but it does play an important role in accelerating the ring cutoff process once the meander has developed. The flat bottom experiment produced essentially the same results as the control experiment. In this two week comparison, the bottom topography seems to be much less important than the presence/absence of dynamic features in the initial condition. As mentioned earlier, the topography has been altered to satisfy quasi-geostrophic constraints and the effects of the bottom topography may be present in the initial position of the Gulf Stream and rings used to initialize the model forecasts.

Control-II was initialized with our best estimate of the conditions of 23 November. All of the major events observed in the IR data were reproduced in this model run. The W_1–N_1 interaction, deep sock meander, and cold ring formation all compare well with the IR data. Time of formation of C_2 is 15 days, close to the shortest possible time in the IR of 17 days. In the eastern portion of the domain, shingle-like activity preceded the birth of a new warm ring on day 20. The time of formation, size, and location of this ring are all in excellent agreement with the IR data. The absorption of ring W_2 and birth of the new ring W_6 is not in disagreement with the observed SST data. Persistent cloud cover between 3 and 24 December did not allow for precise knowledge of the interaction/formation events in that region. The birth of W_5 in Control-II is different from the birth of the analogous ring in experiment 2. The cloud cover in the IR images does not allow us to definitely verify

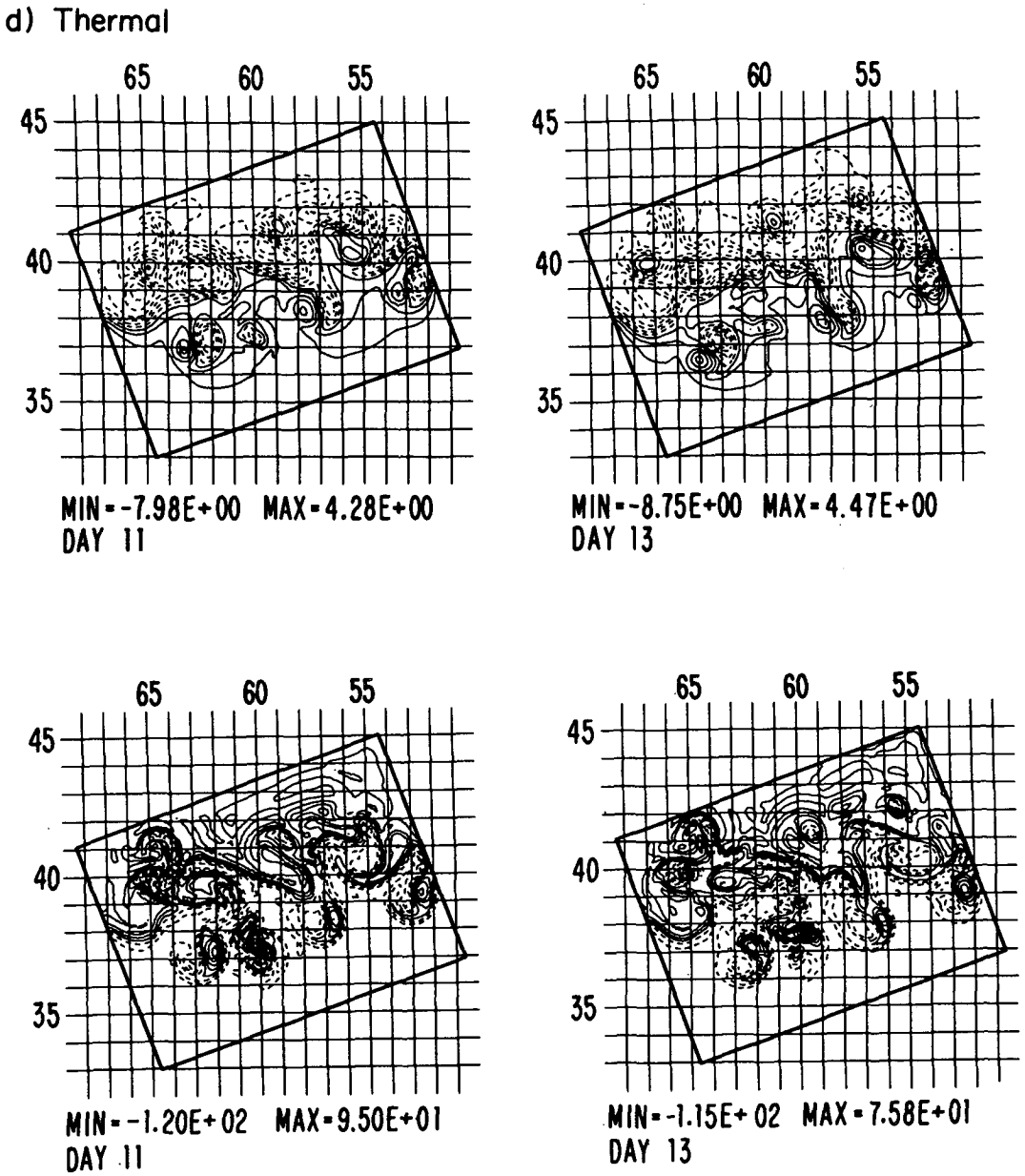

FIG. 14. (*Continued*)

either formation. We know that in experiment 2 W_5 is formed from part of meander N_2 but in Control-II W_5 is formed directly from N_3. Because of this, we believe the formation in Control-II is more realistic.

The sea surface geostrophic density anomaly, ψ_z, is shown in Fig. 12 and can be directly compared with sea surface temperature. Weak shingling activity is visible along the crests of the anticyclonic meanders. The shingle which detached from N_3 at day 8 has a clear surface signature and it is evident that it entrains water from the Gulf Stream. The newly formed warm and cold rings show a very strong surface signature. In this quasi-geostrophic (QG) simulation there is no upper mixed layer, and thus the characteristic covering over of rings is not possible. The warm core rings formed (from N_2 and N_3) are circumvented by slope water which assumes the characteristic shape of shingles wrapping around the rings, as is often seen in the SST data. A multitude of small scales exist in the surface flow that are not observed in the IR data. It is our interest to further investigate this behavior across a large spectrum of model parameters, but it could also be that the NOAA SST analysis used here are smoothed so that the small-scale behavior is eliminated. Atmospheric forcing may also be involved in the mixing of these small scales. These effects can be investigated with

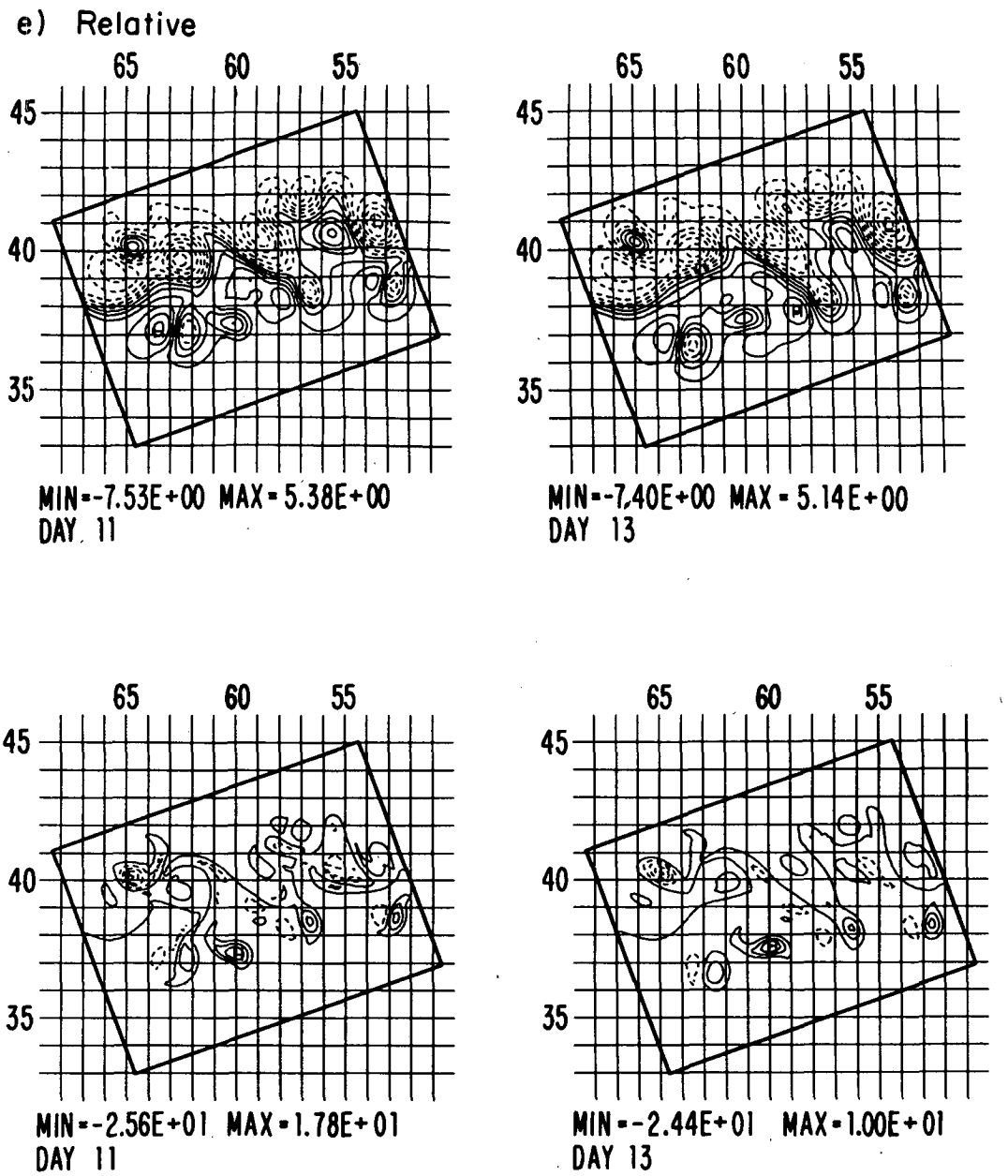

FIG. 14. (*Continued*)

a coupled QG-upper mixed layer model (Walstad 1987).

Other interesting features of the sea surface density anomaly are the warm outbreaks on the Sargasso Sea side of the Stream. On day 12 the warm outbreak seen in the surface density field near 37°N, 63°W is a tongue of warm water advected around the near field anticyclone formed in the upstream part of the meander (Fig. 12). Later, near the same location at day 21, we note that another outbreak has developed, which is not coherent with any subsurface velocity front (compare day 21 of Figs. 11 and 12). Water was pulled off from the stream from a small scale meander on day 15 and afterwards entrained between two near-field anticyclonic eddies. We know that this filamenting patch of water elongates due to the differential advective velocity between the stream and the Sargasso Sea, since here the surface density is simply advected by the underlying velocity field. These outbreaks look very similar to features observed in the SST data (Cornillon et al. 1986). In summary, the sea surface front due to the warm outbreaks could be the signature of a deep field of eddies, which advect the warm sea surface density anomaly as a passive tracer.

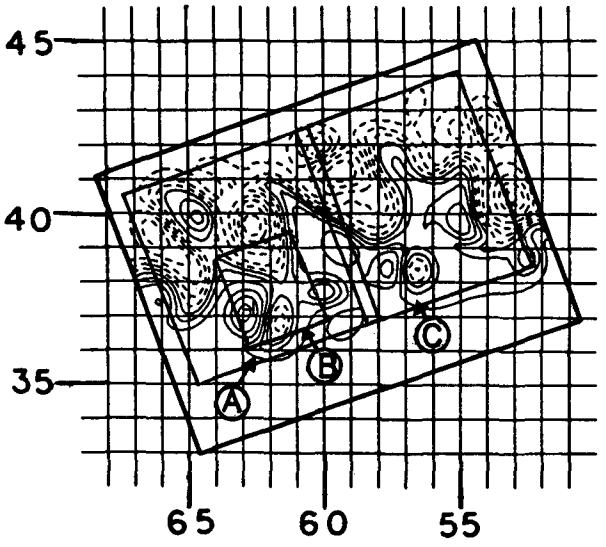

FIG. 15. Subregions used in EVA analysis. A: cold ring EVA, B: cold ring integrated balances, C: warm ring EVA.

The thin tongue of slope water entrained in the S_3 meander of the stream is similar to the signal observed between day 5 and day 10, (Fig. 5b, c), but here a small cold ring is formed while the SST analysis is not conclusive due to cloud cover. All the runs performed show a strong tendency to form a cold ring in this position. It is interesting to note that the new cold core ring detached from S_3 has a strong signature only at 100 and 300 m, much shallower than for ring C_2.

Control-I and Control-II are qualitatively similar but quantitatively different in the ring–stream interaction and C_2 formation region. Comparing these results, we conclude that the different ring Feature–Models used in the initial condition have primarily influenced the C_2 detachment time and the duration of the N_1–W_1 interaction. The newly formed cold core ring C_2 is, however, not appreciably different in its vertical structure in the experiments 1, 2 and 4 so that we conclude that its characteristics depend mostly on the stream structure. However, experiment 1 shows a different W_1–N_1 interaction process than is seen in experiment 4. This is due to the maximum velocity in the initial W_1 ring being at the outer edge of the ring in experiment 1 versus at radius r_0 in experiment 4, (model A for experiment 1 and model B for experiment 4). The former induces strong small scale oscillations of the ring borders and, consequently, a different interaction with N_1. Cushman-Roisin (1986) has shown that for this kind of ring stable oscillations can occur at the ring border and our model exhibits such behavior.

The differences between Control-I and Control-II in the eastern portion of the basin are significant. In control-I there was no clear warm ring formation whereas in Control-II the observed ring W_5 formed in good agreement with the data. The early development appears to be quite similar in both cases, e.g., on day 9 the two fields look qualitatively similar. We believe that the preconditioning shingling activity of the stream could be important to the growth and subsequent pinchoff of a large meander. This occurs in the region of the stream in which the initial shape was modified. Small refinements in the shape of the stream may have a considerable impact on the formation of new rings. Although the three additional small warm rings interact with the stream and new ring W_5, they are not believed to be critical to the warm ring formation process.

Experiments 5 and 6 tested the influence of a small change in the initial position of a nearby warm ring and the effect of persisted boundary conditions on the ring formation process. A small shift in the initial position of W_1 changed the characteristics of the ring–stream interaction and strongly influenced the ring formation process. The meander development is nearly identical to that of Control-II, however the prolonged W_1–N_1 interaction inhibits the cutting off process after day 9. When the boundary conditions are held fixed the strength of W_1–N_1 interaction is greatly reduced. The meander development and ring formation process is very similar to the control experiment. The major difference is in the strength of W_1 and the Gulf Stream position after the interaction weakens. It appears that in this experiment the ring gave up some of its energy to the stream while in the control experiment the ring gained energy from the stream. The fact that the new cold ring still forms indicates that the formation process is dominated by internal dynamics and not by information advected in through the boundary.

6. Dynamical processes

a. Parameter sensitivity experiments

Here we describe a set of experiments to elucidate the role of different dynamical balances in the cutoff process of the cold ring formation as predicted by Control-I (Fig. 7). These parameter/sensitivity experiments were designed to study the role of baroclinicity, nonlinearity, and beta in the cold ring cutoff process. This was accomplished through an artificial enhancement or reduction of selected terms in the vorticity equation. Table 5 contains the list of experiments and the corresponding nondimensional values of α, β and Γ^2 used. To review the terms: α measures nonlinearity, β measures the planetary vorticity, and Γ^2 measures the baroclinicity. The initial conditions are the same as in Fig. 4a, for Control-I. The model was run with the standard parameters of Table 1 up to day 8 and then stopped. Day 8 was chosen because it is the time at which the neck of the deepening meander is forming to break off the cold core ring C_2. The model was restarted after changing the values of the parameters in Eq. (1) so that a different dynamical balance is imposed in the subsequent evolution of the flow field. Figure 14 contains the results from Control-I and four different

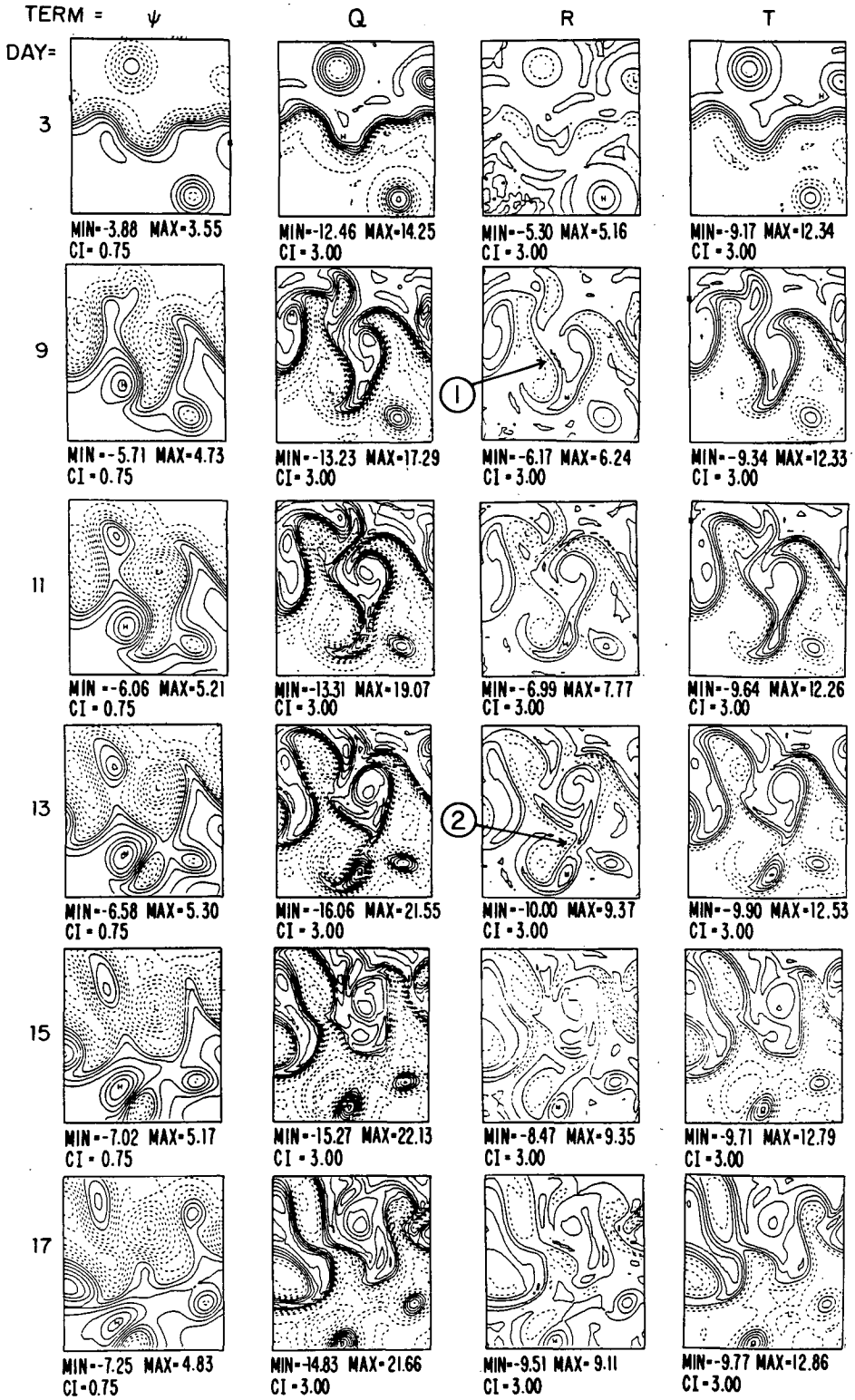

FIG. 16. The streamfunction and vorticity budgets in subregion A (Fig. 15) at 300 m for Control-II. The model day is indicated on the left and the terms are indicated at the top, the symbols are explained in Table 1.

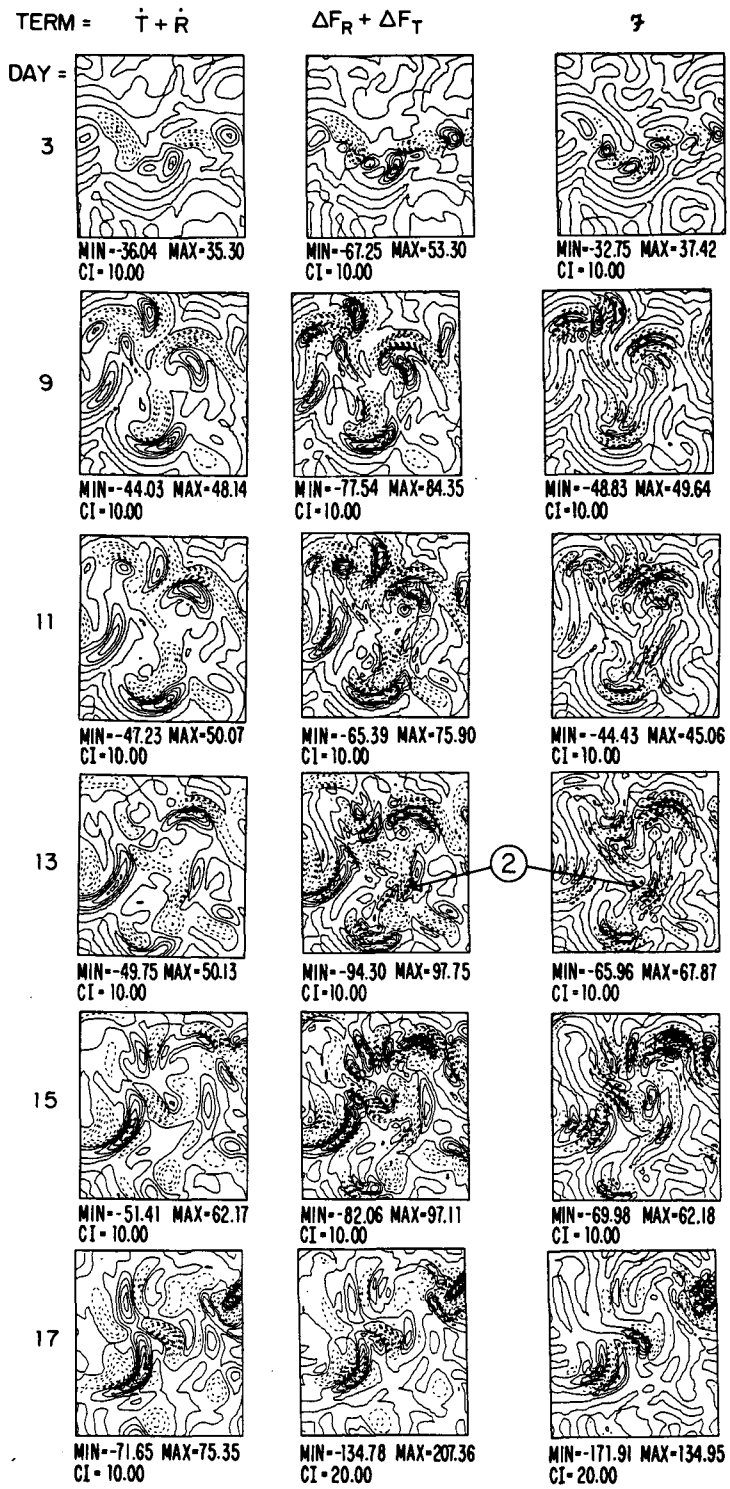

FIG. 17. The vorticity balances in subregion A for Control-II at 300 m. The model day is indicated on the left and the terms are indicated at the top, the symbols are explained in Table 1.

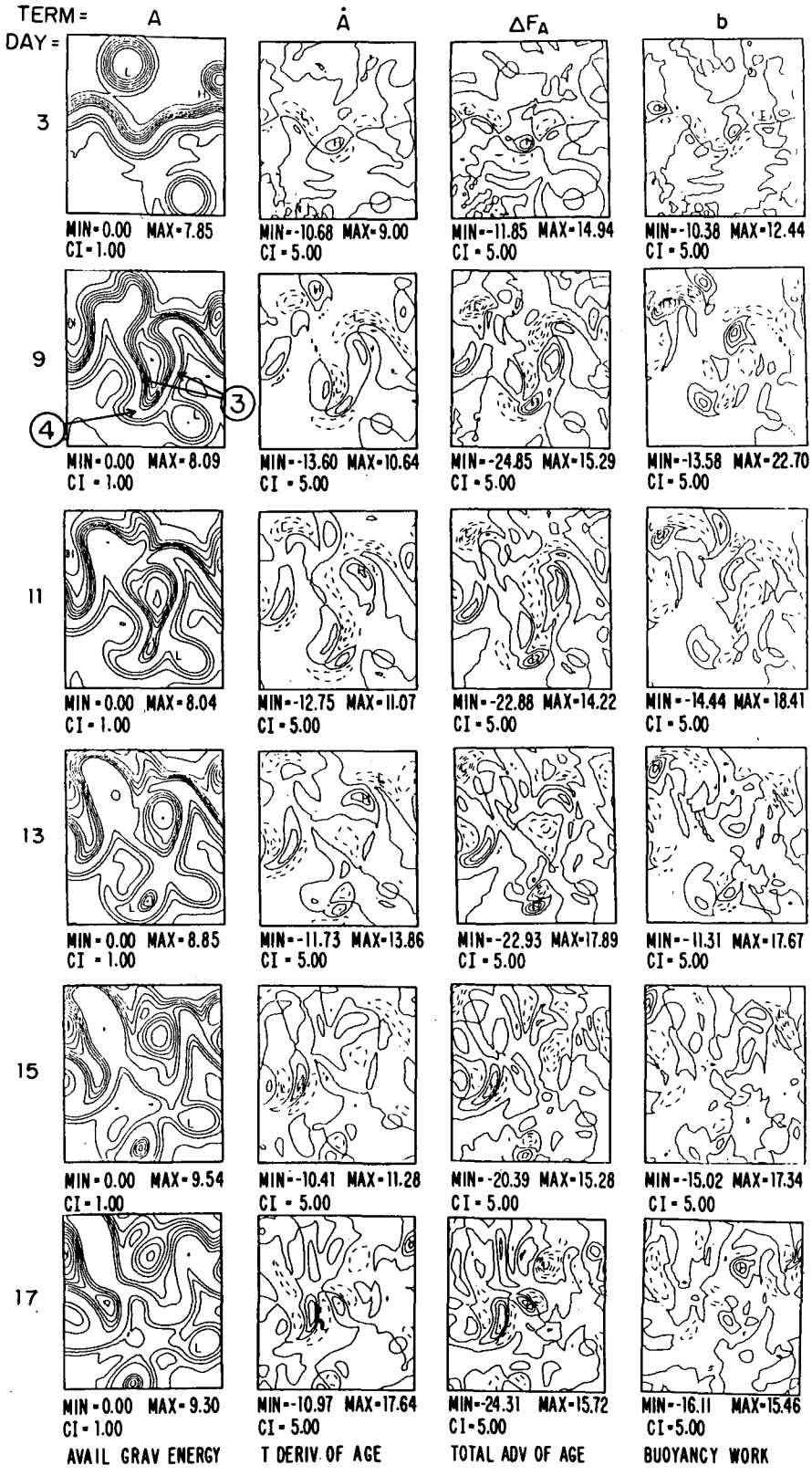

FIG. 18. The available gravitational energy equation balances in subregion A for Control-II at 300 m. The model day is indicated on the left and the terms are indicated at the top, the symbols are explained in Table 1.

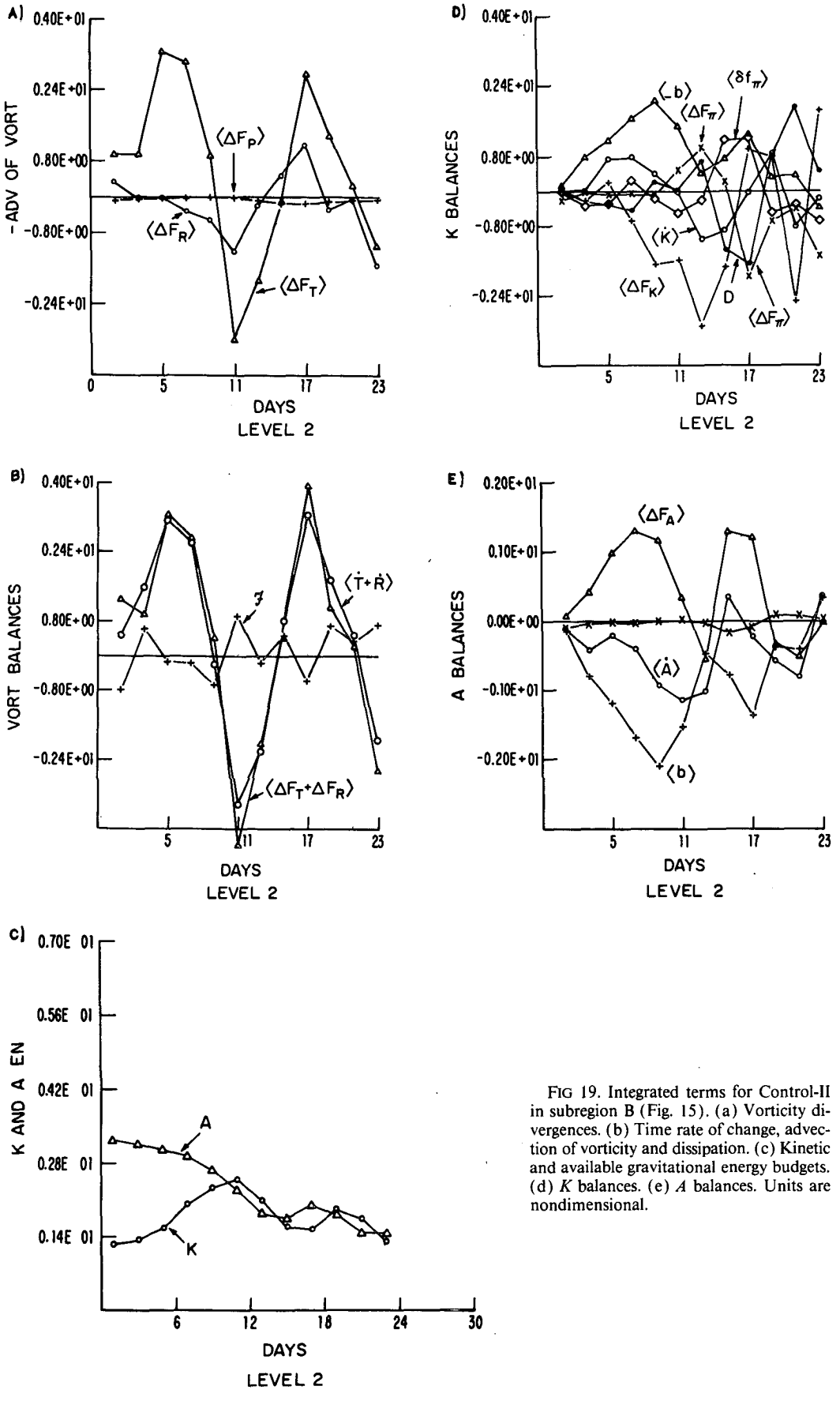

FIG 19. Integrated terms for Control-II in subregion B (Fig. 15). (a) Vorticity divergences. (b) Time rate of change, advection of vorticity and dissipation. (c) Kinetic and available gravitational energy budgets. (d) K balances. (e) A balances. Units are nondimensional.

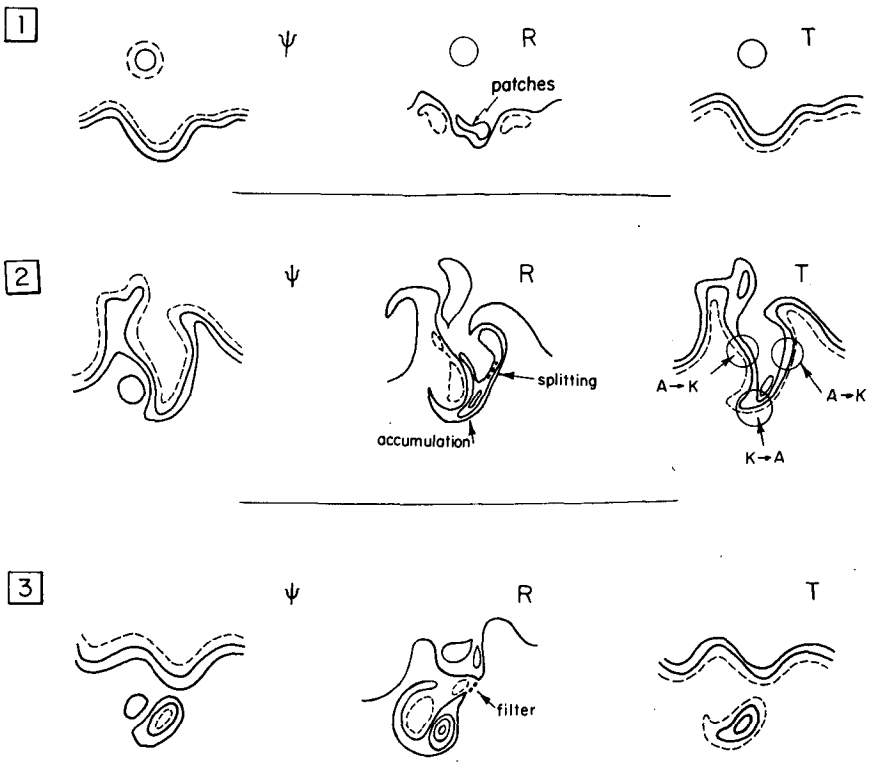

FIG. 20. Schematic of the energy and vorticity processes involved in the cold ring cutoff event: 1), 2), 3) indicate the streamfunction, relative vorticity, and thermal vorticity fields for the three-phase ring formation process.

experiments at days 11 and 13, after restarting the model at day 8.

The nonlinear (b) and linear (c) experiments were designed to study the role of the nonlinear terms in the ring pinchoff process. In experiment (b), Fig. 14b, the nonlinear terms were enhanced by a factor of 3; the ring formation process proceeds very quickly and the new ring is completely formed by day 11. Experiment (c), Fig. 14c, has had the nonlinear terms reduced by a factor of 3; very little development of the meander is seen between day 8 and 13. Experiments (b) and (c) clearly show that the process is triggered and dominated by nonlinear interactions. The thermal (d) and relative (e) experiments show the relative importance of baroclinic versus barotropic effects. Experiment (d), Fig. 14d, shows that the enhanced baroclinic effects are responsible for a slightly faster cutoff of the vorticity field of the ring with respect to the control experiment. In experiment (e), Fig. 14e, the barotropic case, the ring formation is slowed down slightly. The important difference between experiments (d) and (e) is the size of the newly formed ring C_2. The baroclinic ring has higher velocities at its border (a factor of 2 higher than the barotropic case), has a very deep structure (90 cm s^{-1} at 2000 m), and is slightly larger in diameter.

In the final set of parameter experiments the influence of an enhanced β was studied. Experiment (f) had β increased by 10 and experiment (g) had both β increased by 10 and α reduced by a factor of 3. The results are qualitatively the same as for the nominal values of β. There is more small scale meandering in the stream and in experiment (f) the new ring is slightly distorted. These results are not shown here.

In summary, a nonlinear baroclinic process essentially unaffected by the beta effect is indicated.

b. Energy and vorticity analysis

In this section we describe and interpret the energy and vorticity analysis for the cold ring formation C_1 and the warm ring formation W_5 of Control-II. Important terms in these equations, [Eqs. (1b), (2b), (3b)], are displayed in a time series of horizontal maps and subregional integral balances of terms are graphed as time series. The subregions of the model domain in which the EVA analysis were carried out are shown in Fig. 15.

1) COLD RING FORMATION

In Fig. 16, a subregion (domain A in Fig. 15) of the 300 m streamfunction and vorticity field components of Control-II are shown. The vorticity at day 3 is mostly composed of the thermal vorticity, T, with small patches of relative vorticity, R, along the anticyclonic

and cyclonic meanders of the Gulf Stream jet. At day 9, the stream has developed a deep meander; the thermal vorticity is still visually coherent with the streamfunction pattern and the relative vorticity patches have elongated and stretched along the sides of the deepening meander. The coalescence of W_1 and N_1 is evident both in the R and T fields. In the upstream part of the jet meander there are indications of an enstrophy cascade in R to small scales (location 1); note small patches of detached vorticity in the center of the domain. At the bottom of the meander the jet diverges and there is an accumulation of R.

In the dynamic vorticity field Q, by day 11, W_1 vorticity has completely merged with the stream vorticity. The meander has assumed a convoluted shape in both the T and R fields. The patch of vorticity at the bottom of the meander has increased in strength and a narrow neck region is forming above it. The Q and R have formed closed contours in the lower neck region but ψ and T have not.

At day 13, several T and ψ contours have broken off in a separate patch. The R is still attached to the stream vorticity but there is evidence of an enstrophy cascade at the neck (location 2). The near field anticyclone is advecting the base of the meander causing the long filamenting tail in the southwest quadrant. The magnitude of R in the pinching ring has more than doubled since the meander began to develop. Only later, on day 17, both R and Q break completely, carrying the anticyclone away with the new ring.

The vorticity balances are shown in Fig. 17. The planetary vorticity advection is neglected since, locally, it is numerically unimportant. At day 3, each of the fields show multipolar structures (high/low extrema pair) along the meandering jet. The $\dot{R} + \dot{T}$ exists at the larger scales of the $\Delta F_R + \Delta F_T$ fields which exhibit also the smaller scales shared with the filter, F. The filter is active all along the jet during the first adjustment phase. At day 9, the local nonlinear interactions are well developed at the two meander crests (N_1 and N_2) and the trough (S_2) and they are partially balanced by the filter. The picture on day 11 is quite similar with some activity developing at the neck region in all three terms. On day 13 the neck is the site of strong nonlinear interactions and dissipation by the filter, location 2. This is where the cascade in R was occurring in Fig. 16.

In summary, prior to the event of cold ring cutoff the vorticity field contains a convoluted pattern of filaments and small scale relative vorticity embedded in a larger scale thermal vorticity. The local vorticity balances in the deepening meander show strong nonlinear interactions at the meander crests and troughs and an intense cascade of R along the upstream meander jet and at the neck. The neck is a region of high velocity and steep vorticity gradients at which the filter dissipates the enstrophy cascading to small scales. The bottom of the meander is instead a region of decreasing velocity, or divergence, due to the wrapping of the meander around the southern border of the near-field eddy. The nonlinear terms cause a net accumulation of R here.

The available gravitational energy (A) and its balance [Eq. (3b)] at 300 m are shown in Fig. 18 for Control-II. On day 3, the axis of the jet is characterized by a low in A, this is because the density surfaces of the Feature–Model are unperturbed from the motionless state at the center of the stream. The slope and Sargasso Sea sides are both regions of large density anomalies and thus large A. Again we see the characteristic multipolar structure in $\dot{A}$, ΔF_A, and b along the jet. At day 9 the sides of the meander (location 3) are the site of positive ΔF_A energy flux divergences. This net accumulation of A is partly converted to K via buoyancy work b along the jetlike borders of the meander. Near the bottom of the meander (location 4) the net contribution from b and the positive ΔF_A energy flux divergence contributes to the accumulation of A. Processwise, the accumulation of vorticity at the bottom of the meander triggers a conversion from K to A, typical of finite amplitude barotropic instability processes (Pinardi and Robinson 1986). Horizontal advections and b are decreasing A at the very base and in the central region of the meander as it extends to the south and begins to form the narrow neck. The maximum baroclinic energy conversion from A to K along the meander jets is at day 11. During the actual pinching event, both ΔF_A and b are small along the meander jets and at the neck. After the ring has pinched off (day 15) the balance is mostly between the $\dot{A}$ and ΔF_A terms in the location of the detached ring.

The K balances are not shown because they do not add any new insights to the process understanding already emerging from the A and Q balances. The outstanding process in the K equation [Eq. (2b)] is the accumulation of K at the bottom of the meander via ΔF_K and ΔF_π.

The horizontally integrated vorticity and energy budgets at 300 m are shown in Fig. 19; here the angle brackets indicate the average value of any quantity in the subdomain centered on the western meander jet, domain B in Fig. 15. Figure 19a shows the advection terms in the region of the meander jets. The major changes occur in the $\langle \Delta F_T \rangle$ term before day 11, $\langle \Delta F_P \rangle$ is practically negligible and $\langle \Delta F_R \rangle$ has the same behavior of the nonlinear stretching term but at smaller amplitude. The vorticity balances (Fig. 19b) show the rapid change in the tendencies of Q before the pinching of the cold core (day 11) and the enhancement of the filter (F) during the cutoff phase.

Figure 19c shows the K and A budgets: K increases at the expense of A until day 11 then it decreases again, primarily due to horizontal advections. Figure 19d shows the K balances and Fig. 19e the A balances. Before ring formation, days 0–11, the kinetic energy balances are dominated at this level by $\langle -b \rangle$ which in-

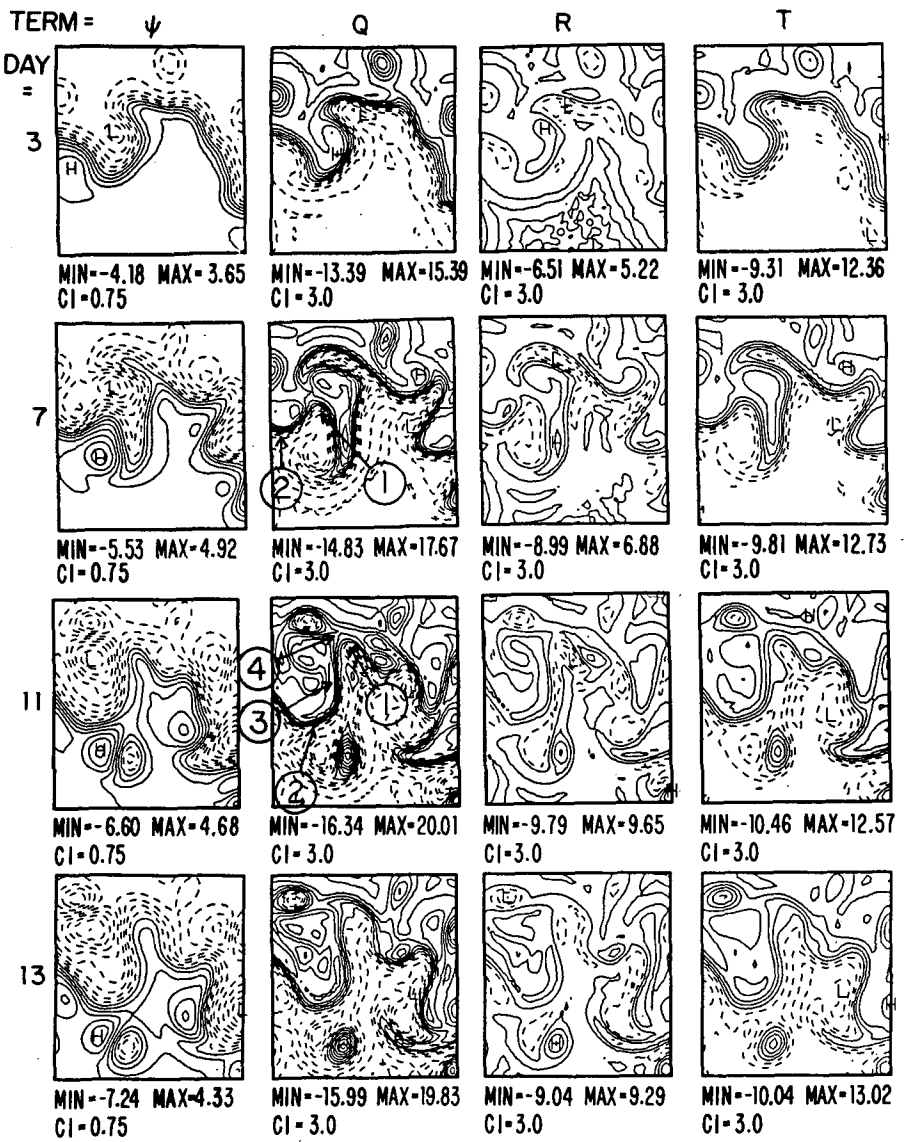

FIG. 21. The streamfunction and vorticity budgets in subregion C (Fig. 15) at 300 m for Control-II. The model day is indicated on the left and the terms are indicated at the top; the symbols are explained in Table 1.

creases the K of the meander jet, and by $\langle \Delta F_K \rangle$ which transports energy away from this region. At the moment of the pinch-off $\langle \Delta F_\pi \rangle$ and $\langle \Delta f_\pi \rangle$ grow positive definite and partially balanced by a negative $\langle \Delta F_k \rangle$.

At other levels, the balances show the same tendencies but with an enhanced role played by $\langle \delta f_\pi \rangle$ (positive at 100 m and negative at 700 m). The A balances are dominated by the negative tendency in $\langle \dot{A} \rangle$ as a result of the net conversion of A via $\langle b \rangle$ into K which overwhelms the positive heat flux divergences ($\langle \Delta F_A \rangle$). All the other upper thermocline levels show the same tendencies in this equation.

In conclusion, we present a schematic of the pinching process in Fig. 20. The streamfunction and components of the vorticity (R and T) are shown for the three-phase process. During phase 1, the meandering of the stream develops; in the anticyclonic and cyclonic curvature regions of the stream small amplitude patches of R are embedded in the large scale T field. During phase 2, the meander has deepened and in the vorticity field there is a net accumulation of R and T at the bottom of the meander. An enstrophy cascade develops that splits the R patches along the meander side jets. There are energy conversions $A \rightarrow K$ in the meander jets and $K \rightarrow A$ at the bottom of the meander. Finally, during the third phase, T breaks in a separate patch and the final cutoff of R is produced by the dissipative-like effects in the model at the position of the maximum

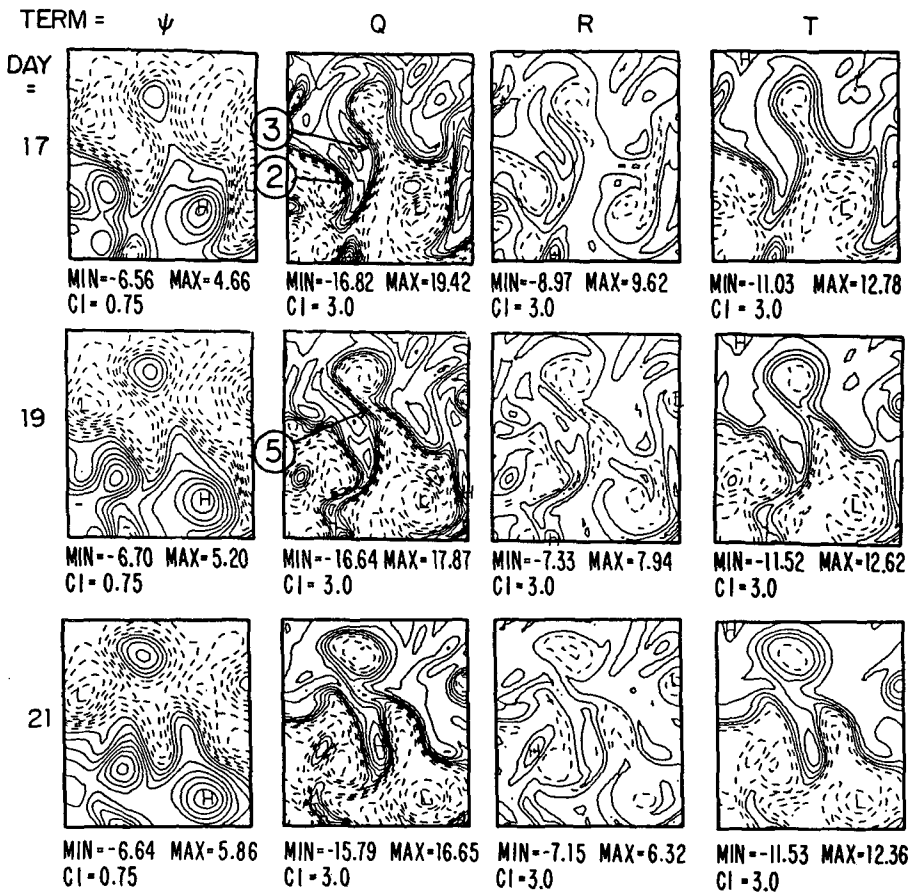

FIG. 21. (*Continued*)

enstrophy cascade. The result of this process is that a patch of vorticity from the northern side of the stream (continuous lines in the T field) separates to the south of the Gulf Stream jet.

2) WARM RING FORMATION

In this section we will discuss the W_5 formation in Control-II. The formation event may be separated into three different phases: preconditioning (days 0–9); growth, (days 9–13); and cutoff (days 15–21). The preconditioning phase sets up the stream for rapid meander growth via small scale meandering of the Gulf Stream front and birth of a cold ring and shingle. This process develops slowly over the first 9 days. In the growth phase, a small bump in the meandering stream amplifies into a large looping meander. This growth is very rapid, occurring in only 4 days. The final phase of ring cutoff is achieved by the eastward propagation of a small meander overtaking the fully developed looping meander. This cutoff process is much slower than the cold ring cutoff and takes about 6 days.

A subregion of the vorticity and streamfunction fields (domain C in Fig. 15) for the W_5 formation is shown in Fig. 21. During the preconditioning phase, a shingle-like feature and small cold ring are formed and the stream develops a small scale meandering. On day 3 the dynamic vorticity is mostly composed of T with contributions from R in patches along the jet. By day 7, the thin filament of Gulf Stream water which forms the shingle-like feature is clearly evident in each of the fields. The R field has elongated along the meandering stream while T is still coherent with ψ. The shingle has an associated near field cyclonic eddy which is clearly evident on the upstream part of the meander. A very sharp trough has developed near the center of the domain. This is the location of the small cold ring (C_3) formation on day 9 (not shown). After the C_3 formation, the upstream crest (location 1) will develop into the small bump of the second phase. A trough is just entering the domain at location 2. The cold ring cutoff and shingle formation processes have all the same vorticity characteristics as the cold ring formation discussed in the previous section.

The second phase is characterized by rapid growth of a looping meander and sharp frontal steepening of the Gulf Stream. On day 11 the shingle has almost separated and the small bump which remained after

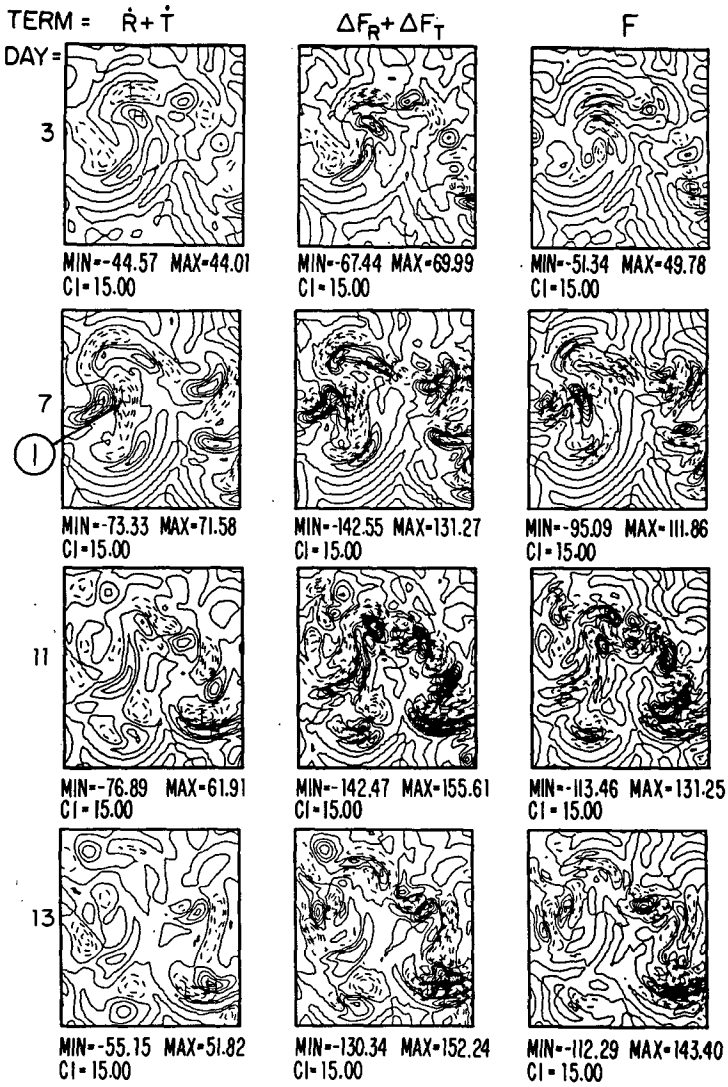

FIG. 22. The vorticity balances in subregion C for Control-II at 300 m. The model day is indicated on the left and the terms are indicated at the top; the symbols are explained in Table 1.

the cold ring formation has propagated and begun to grow (location 1). The bump is most visible in the T field, while the R field is composed of small patches. The upstream side of the growing meander (location 3) develops a north–south orientation through the eastward propagation of the upstream trough and an effective blocking of the crest of the meander via its interaction with the newly formed shingle (location 4). The bump continues to amplify and has doubled in size by day 13. Here T is the dominant form of vorticity in the developing meander while R has actually decreased throughout the growth phase.

The cutoff of the developed meander is caused by the rapidly propagating stream trough (location 2), which advects the base of the forming warm ring to the east (location 3), causing the neck to close off. On day 17 two ψ contours have closed off but no contours have closed in the vorticity fields and R is still very small. At day 19, the rapid translation of the upstream trough is evident; Q, R and T have accumulated in the southern trough and there are indications of a small nonlinear cascade of R along the frontal area and in the neck region (location 5). Day 21 shows a strong warm ring separated from the stream, connected only by a thin filament of vorticity at the neck. The newly formed ring begins to interact with the upstream crest as the meander continues to propagate to the east. Throughout the warm ring formation, the vorticity has been mostly composed of T. There was no large accumulation of R at the top of the meander in the forming ring.

Selected components of the vorticity equation are

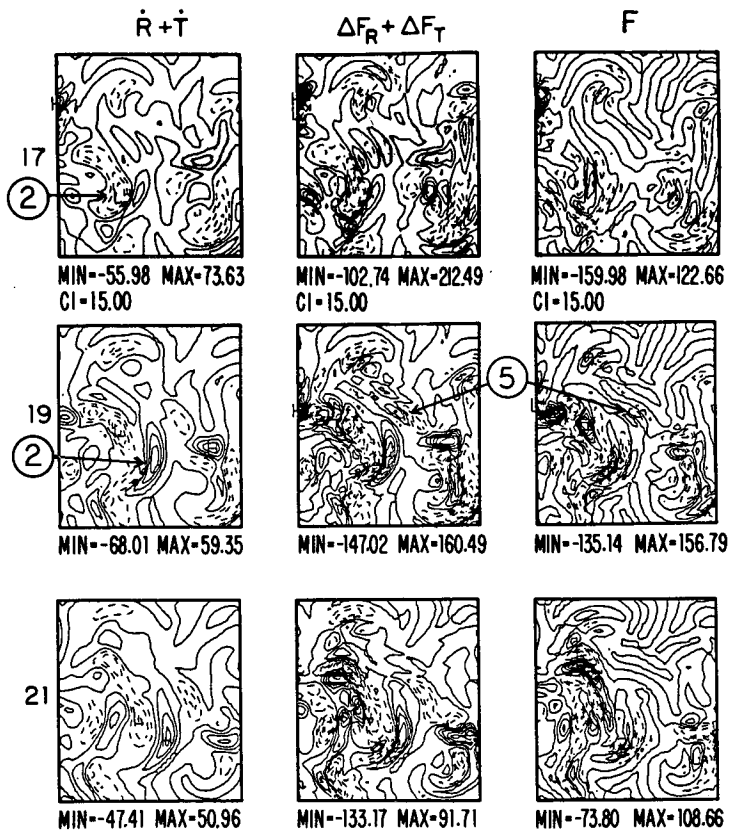

FIG. 22. (*Continued*)

shown in Fig. 22 for the warm ring formation. During the preconditioning phase, days 3–9, both the nonlinear terms and the filter contribute to the shingling activity and cold ring formation. This is characteristic of the cold ring formation process discussed in the previous section. The vorticity is decreasing very rapidly on day 7 in the developing bump in the stream (location 1), primarily due to horizontal advections. Throughout the early growth period (day 11) the vorticity is changing rapidly due to advection (mostly ΔF_R) and filter processes. On day 13, $\Delta F_R + \Delta F_T$ and F decrease in magnitude and are nearly in balance, resulting in very little change in the vorticity field of the large loop. This marks the end of the growth phase. The early part of the cut-off phase, days 13–17, is characterized by slow evolution, small nonlinear terms, and very little filtering activity in the looping meander. At the upstream trough (location 2) the signature of the eastward propagating meander is clearly visible in the time rate of change of the vorticity, balanced by strong $\Delta F_R + \Delta F_T$. The final cutoff is achieved as this meander overtakes the nearly stationary looping meander, advecting the base of the meander to the east. As the final separation occurs, day 19, the nonlinear terms and filter increase slightly in the neck (location 5).

The available gravitational energy terms for the warm ring formation are shown in Fig. 23. The locations of negative $\dot{A}$ on day 3 indicate the stream axis is shifting into the regions where the shingle and cold ring form. Both horizontal advections and buoyancy conversions contribute to this formation. On day 7 the shingle is very elongated, still being driven by ΔF_A and b. At the crest just upstream ΔF_A and b are decreasing A, an indication of the developing bump (location 1). The eastward propagation of the upstream trough and rapid development of the small bump during the growth phase are evident on days 11 and 13, at locations 2 and 1, respectively. Once again, during the cutoff phase there is very little activity in the region of the forming ring but strong horizontal advections are occurring at the upstream trough. The eastward propagation of the trough is visible in the $\dot{A}$ terms (location 2 on day 17), primarily driven by the horizontal advections. On day 21 there is a large patch of A separated to the north of the eastward propagating meander and the ring is beginning to interact with the upstream crest.

The schematic in Fig. 24 shows the position of the front encompassing the maximum velocity core of the Gulf Stream during the three phase process of ring formation. In each picture, the shaded stream indicates its position at the beginning of the phase, the unshaded stream indicates the position at the end of the phase. The first picture indicates the major events that occur during the preconditioning phase: birth of the shingle

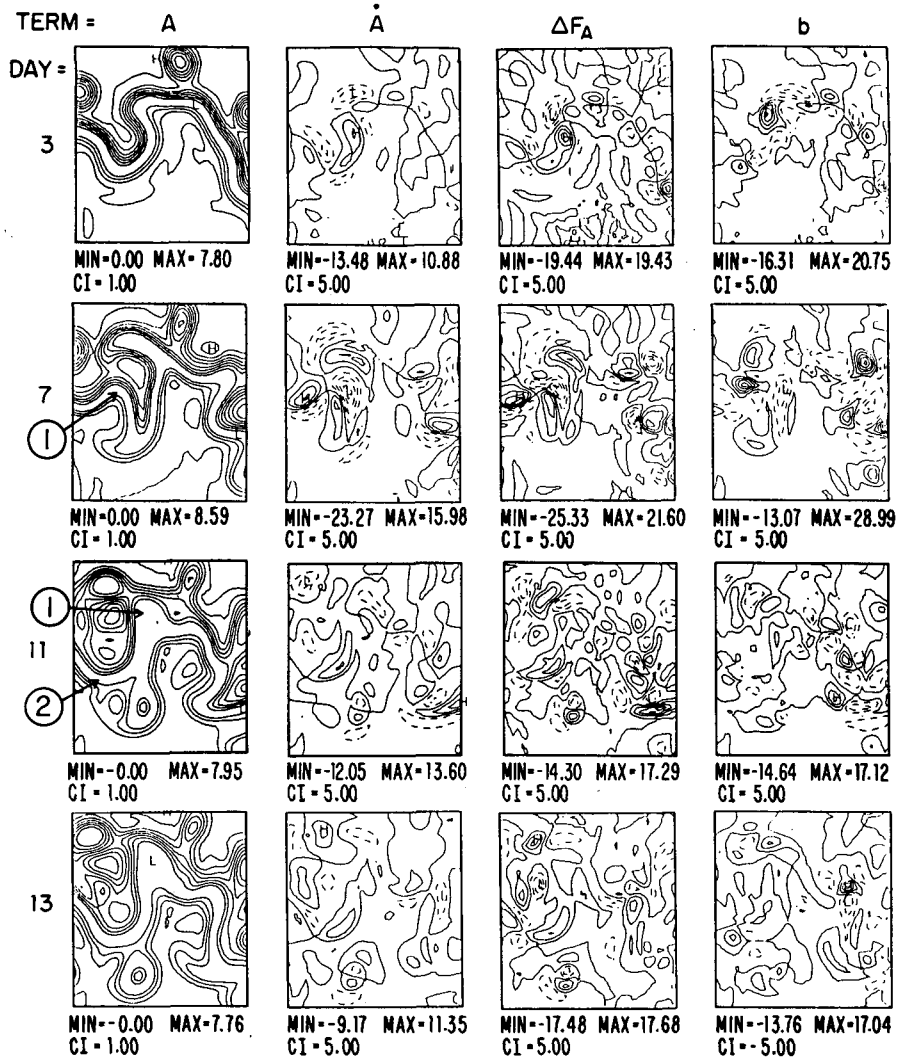

FIG. 23. The available gravitational energy equation balances in subregion C for Control-II at 300 m. The model day is indicated on the left and the terms are indicated along the top, the symbols are explained in Table 1.

from N_3 and cold ring C_3 from S_3; and propagation of the upstream meander crest after the cutoff of C_3. During this phase strong nonlinear interactions are acting along N_3 and S_3; F cuts off the neck of the shingle and cold ring. The ΔF_A and b contributions are important, producing the same accumulation and splitting processes that occurred in the formation of C_2. The second schematic depicts the two major events during the growth phase: rapid growth of the meander crest into a large loop of the current; and steepening of the frontal region between the upstream trough and the developing loop. During this phase the nonlinear interactions decrease in magnitude. The major amplification process of the stream loop is driven by ΔF_R and F, e.g., horizontal redistribution processes. However, the frontal area and the trough upstream of the growing meander is the location of strong baroclinic stretching processes which maintain the front until the end of the cutoff phase. During the third phase, eastward propagation of the trough due to ΔF_R, ΔF_T and ΔF_A overtakes the nearly stationary looping meander and produces filamenting of the vorticity field in the neck of the forming warm core ring, trapping the Sargasso Sea side vorticity. No strong accumulation of R occurs during the cutoff phase so that the interior of the ring is mainly composed of the Sargasso Sea vorticity near the front after the growth phase.

These results show that the birth of a warm core ring results from the amplification of a small scale perturbation, which is advected along a preexisting large meander of the Gulf Stream front. The process of growth of the new ring is dominated by horizontal re-

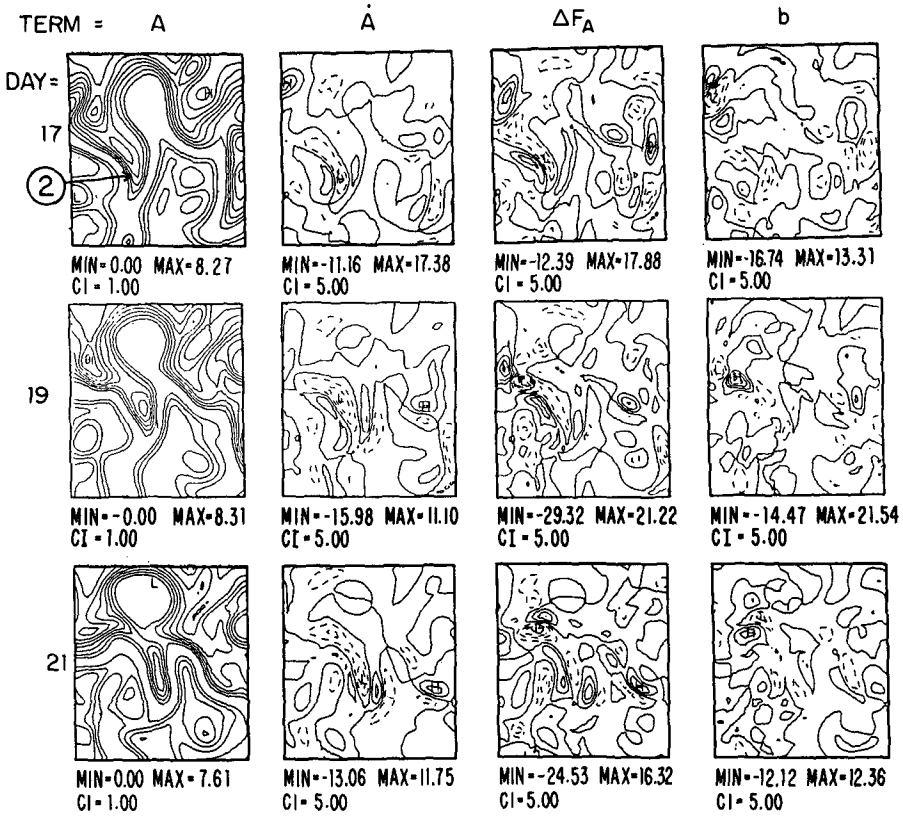

FIG. 23. (*Continued*)

distribution processes in the meander anticyclonic core and the pinch-off is produced by differential advection of the crest and trough of the developed meander.

7. Summary and conclusions

We have carried out a study of the Gulf Stream Meander and Ring (GSMR) region in terms of numerical simulations via a baroclinic quasi-geostrophic open-ocean dynamical model based upon a month of observations during the period November–December 1984. Research issues include: (i) the synoptic–descriptive oceanography of the GSMR region, (ii) the local dynamics (physics governing the synoptic–dynamical events), (iii) the methodologies of simulations, dynamical interpolations (vertically, horizontally, and temporally) and of dynamical prediction, and (iv) the validation and calibration of the dynamical model. Regional events and processes of importance involve (multiple) ring–ring and ring–stream interactions including: ring formations via meander breakoffs; ring coalescences with the stream; ring–ring mergers, interactions, and contacts. Simulations generate large datasets that require a substantial research effort in descriptive and dynamical analysis for interpretation and evaluation. Comparisons of simulated and observed events are involved and must deal with questions of (space–time) phase errors. The data itself is superficial, gappy, and, to some extent, even eventwise ambiguous. The methodology of Feature–Model initialization was introduced to exploit satellite observed (stream and ring) frontal segments via dynamical model assimilation. Initial condition, boundary condition, and parameter-sensitivity studies were utilized to explore the role of processes and for model calibration. Detailed energy and vorticity analysis (EVA) were carried out to elucidate the physical processes governing a major cold-core and a major warm-core ring generation event.

The observational database is summarized in Fig. 5 and the associated synoptic–dynamical events are schematized in Fig. 6 (NOAA Analysis) and described in Table 3 (NOAA Analysis). The model parameters are presented in Table 1. The design of the simulation experiments is summarized in Table 4 with the initial conditions displayed in Fig. 4 and the results schematized in Fig. 6 and described in Table 3. The discussion and intercomparison of results are found in section 5b. Table 5 is the design and Fig. 14 the results for the parameter and sensitivity study which indicates a dominance of nonlinear baroclinic processes. Sche-

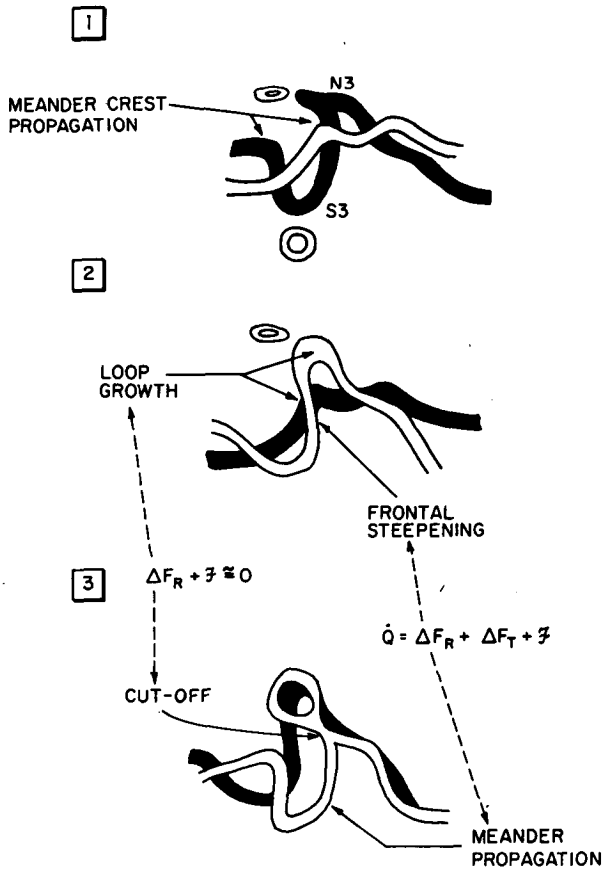

FIG. 24. Schematic of the vorticity processes involved in the three-phase warm ring cutoff event. The shaded and light patterns represent the stream position of the beginning and end of each phase, respectively.

matic maps of the EVA studies of the cold and warm ring births are presented respectively in Fig. 19 and Fig. 24.

The simulations of almost four weeks duration represent the naturally occurring synoptic–dynamical events in the database well, including major cold and warm core ring formations. Feature–Model initialization leads to successful dynamical interpolations: after a few days the structures of stream and ring flows are realistic and the fields have filled in and developed near-field eddies, deep flows, and near surface features. The quasi-geostrophic dynamical model is definitely relevant for the evolution of the thermocline flow in the GSMR region, on the time scales of a few weeks and inclusive of a variety of (energetic) ring and stream interaction events. To the extent that strong topographic interactions (which are not modeled here) are important, they may be built in to the simulations via realistic initial (and boundary) conditions.

Cold and warm core rings appear to be of fundamental dynamical importance to the physical processes governing the GSMR region. This is attested to by (i) their presence, (ii) their role in balance of terms studies carried out, and (iii) their rapid generation in the simulation experiment initialized without rings. Two distinct dynamical processes were revealed by the cold-core and warm-core ring formation case analyses. The cold ring formed in about a week when the neck region (the site of an enstrophy cascade) pinched off a deep meander in which available potential energy was being converted to kinetic energy in the two meander side jets but in which the inverse cascade was occurring at the bottom of the meander. The warm ring formed in about two weeks and was cut off by a differential advection mechanism in which the leading edge of a northward loop was relatively stationary; the loop had already been amplified by a strong horizontal advection of relative vorticity. The generality of the processes revealed in these case studies must be evaluated later.

The results presented here have served as the basis for the development of a real time nowcast and forecast scheme (Robinson 1987; Robinson et al. 1987; Glenn et al. 1987) called GULFCASTING, which involves Feature–Model initialization and updating with satellite IR in the GSMR region but also an in situ database component consisting of AXBT flights. Simulations and forecasting will benefit from the development and/or implementation of data assimilation methodology. Research directions for process and dynamical model studies include topographic interactions and primitive equation dynamics.

Acknowledgments. The support of this research by the Office of Naval Research under Contract N0014-84-C-0461 to Harvard University is gratefully acknowledged. Substantial use was made of the Cyber 205 at the Fleet Numerical Oceanographic Center in Monterey with helpful support in logistics from the FNOC staff. Some calculations were carried out remotely at the Woods Hole Oceanographic Institution and we thank Prof. N. P. Fofonoff for helpful arrangements.

REFERENCES

Bower, A. S., H. T. Rossby and J. L. Lillibridge, 1985: The Gulf Stream—barrier or blender? *J. Phys. Oceanogr.*, **15**, 24–32.

Cornillon, P., D. Evans and W. Large, 1986: Warm outbreaks of the Gulf Stream into the Sargasso Sea. *J. Geophys. Res.*, **91**, 6583–6596.

Cushman-Roisin, B., 1986: Linear stability of large, elliptical warm core rings. *J. Phys. Oceanogr.*, **16**, 1158–1164.

Fofonoff, N. P., and M. M. Hall, 1983: Estimates of mass, momentum and kinetic energy fluxes of the Gulf Stream. *J. Phys. Oceanogr.*, **13**, 1868–1877.

Glenn, S. G., A. R. Robinson and M. A. Spall, 1987: Recent results from the Harvard Gulf Stream Forecasting Program. *Oceanographic Monthly Summary*, **7**, no. 4.

Halkin, D., and T. Rossby, 1985: The structure and transport of the Gulf Stream at 73°W. *J. Phys. Oceanogr.*, **15**, 1439–1452.

Hall, M. M., 1986: Horizontal and vertical structure of the Gulf Stream velocity field at 68°W. *J. Phys. Oceanogr.*, **15**, 1814–1828.

Holland, W. R., and D. B. Haidvogel, 1980: A parameter study of the mixed instability of idealized ocean currents. *Dyn. Atmos. Oceans,* **4,** 185–215.

Ikeda, M., 1981: Meanders and detached eddies of a strong eastward—flowing jet using a two-layer quasi-geostrophic model. *J. Phys. Oceanogr.,* **11,** 526–540.

——, and J. R. Apel, 1981: Mesoscale eddies detached from spatially growing meanders in an eastward-flowing oceanic jet using a two-layer quasigeostrophic model. *J. Phys. Oceanogr.,* **11,** 1638–1661.

Joyce, T. M., 1984: Velocity and hydrographic structure of a Gulf Stream warm core ring. *J. Phys. Oceanogr.,* **14,** 936–947.

Levitus, S., and Oort, A. H., 1977: Global analysis of oceanographic data. *Bull. Amer. Meteor. Soc.,* **59,** 1270–1284.

McHugh, P., and J. Clark, Eds., 1984: Oceanographic analysis Gulf Stream region. *Oceanogr. Mon. Sum.,* **4,** 11–12.

Miller, R. N., A. R. Robinson and D. B. Haidvogel, 1983: A baroclinic quasi-geostrophic open ocean model. *J. Comput. Phys.,* **50,** 38–70.

Niiler, P. P., and A. R. Robinson, 1967: The theory of free inertial jets. II. A numerical experiment for the path of the Gulf Stream. *Tellus,* **19,** 601–619.

Olson, D. B., 1980: The physical oceanography of two rings observed by the cyclonic ring experiment. Part II: Dynamics. *J. Phys. Oceanogr.,* **10,** 514–528.

Pinardi, N., and A. R. Robinson, 1986: Quasigeostrophic energetics of open ocean regions. *Dyn. Atmos. Oceans,* **10,** 185–219.

Pratt, L. J., and M. E. Stern, 1986: Dynamics of potential vorticity fronts and eddy detachment. *J. Phys. Oceanogr.,* **16,** 1101–1120.

Richardson, P. L., 1983: Gulf Stream rings. Eddies in Marine Science, A. R. Robinson, Ed., Springer-Verlag, 19–43.

Robinson, A. R., 1987: Predicting ocean currents, fronts, and eddies. *Three-Dimensional Models of Marine and Estuarine Dynamics,* J. C. J. Nihoul, and B. M. Jamart, Eds., Elsevier Science, 89–111.

——, and L. J. Walstad, 1987: The Harvard Open Ocean Model: Calibration and application to dynamical process, forecasting, and data assimilation studies. *J. App. Num. Math.,* in press.

——, J. R. Luyten, and F. C. Fuglister, 1974: Transient Gulf Stream meandering. Part I: An observational experiment. *J. Phys. Oceanogr.,* **4,** 237–255.

——, J. A. Carton, N. Pinardi and C. N. K. Mooers, 1986: Dynamical forecasting and dynamical interpolation: An experiment in the California current. *J. Phys. Oceanogr.,* **13,** 1561–1579.

——, M. A. Spall, W. G. Leslie, L. J. Walstad and D. J. McGillicuddy, 1987: Gulfcasting: Dynamical forecast experiments for Gulf Stream rings and meanders, November 1985–June 1986. *Harvard Ocean Model Rep.,* 22, Harvard University.

Shapiro, R., 1970: Smoothing, filtering, and boundary effects. *Rev. Geophys. Space Phys.,* **8,** 359–386.

Stern, M. E., 1985: Lateral wave breaking and "shingle" formation in large-scale shear flow. *J. Phys. Oceanogr.,* **15,** 1274–1283.

Walstad, L. J., 1987: Modeling and forecasting deep ocean and near surface mesoscale eddies. Harvard Ph.D. thesis.

Watts, D. R., 1983: Gulf Stream variability. Eddies in Marine Science, A. R. Robinson, Ed., Springer-Verlag, 114–143.

——, and W. E. Johns, 1982: Gulf Stream meanders: Observations on propagation and growth. *J. Geophys. Res.,* **87,** 9467–9476.

Notice to Authors: One of the following statements, whichever is appropriate, must be signed by all authors of a manuscript and received by the Chief Editor before the manuscript can be accepted for publication. See "Information for Contributors," cover page 2. Requests for further information should be addressed to the American Meteorological Society, 45 Beacon Street, Boston, Mass. 02108.

AGREEMENT TO TRANSFER COPYRIGHT

(For non-U.S. Government manuscripts)

Copyright to the article entitled _____
Print

_____

by _____
Print

_____ is hereby assigned and transferred exclusively to the American Meteorological Society (hereinafter referred to as "AMS") effective if and when the article is accepted for publication in

_____
Print

or in any other AMS journal in which the article may be published with the authors' consent. The authors, however, reserve (1) all proprietary rights other than copyright, such as patent rights, and (2) the right to use all or part of this article in future lectures, press releases, and reviews of their own. Certain additional reproduction rights are granted by sections 107 and 108 of the U.S. Copyright Law. All other uses will be subject to the limitations given in the copyright statement of the AMS journal in which the article is published. To be signed by all authors or, if the manuscript is a "work made for hire," by the employer, who is the "legal author" under the U.S. Copyright Law.

Signature	Signature
Print name	Print name
Title if signed by employer	Title if signed by employer
Date	Date
Signature	Signature
Print name	Print name
Title if signed by employer	Title if signed by employer
Date	Date

NOTE: The form below is to be used for a U.S. Government work only if it is precluded from the copyright transfer agreement above.

CERTIFICATION OF U.S. GOVERNMENT MANUSCRIPT

The article entitled _____
Print

_____

by _____
Print

is hereby certified to be a work of the United States Government, to have been prepared by the author(s) as officer(s) or employee(s) of the United States Government as part of the author(s) official duties, and therefore to be precluded from copyright protection. It is further certified that the article has not been published previously in any language and it is agreed to promptly notify the Chief Editor if the manuscript is submitted for publication elsewhere before its disposition by the American Meteorological Society.

Signature (author or employer)	Signature (author or employer)
Print name	Print name
Title if signed by employer	Title if signed by employer
U.S. Government Agency	U.S. Government Agency
Date	Date
Signature (author or employer)	Signature (author or employer)
Print name	Print name
Title if signed by employer	Title if signed by employer
U.S. Government Agency	U.S. Government Agency
Date	Date